Structural insight into the stabilization of microtubules by taxanes

Andrea E. Prota[1*]; Daniel Lucena-Agell[2¤]; Yuntao Ma[3¤]; Juan Estévez-Gallego[2]; Shuo Li[3]; Katja Bargsten[1+]; Fernando Josa-Prado[2], Karl-Heinz Altmann[4]; Natacha Gaillard[1]; Shinji Kamimura[5]; Tobias Mühlethaler[1]; Federico Gago[6]; María A. Oliva.[2]; Michel O. Steinmetz[1,7]; Wei-Shuo Fang[3*]; J. Fernando Díaz[2*].

[1]Laboratory of Biomolecular Research, Division of Biology and Chemistry, Paul Scherrer Institut, CH-5232 Villigen PSI, Switzerland

[2]Centro de Investigaciones Biológicas Margarita Salas, Consejo Superior de Investigaciones Científicas, Ramiro de Maeztu 9, 28040 Madrid, Spain

[3]State Key Laboratory of Bioactive Substances and Functions of Natural Medicines, Institute of Materia Medica, Chinese Academy of Medical Sciences & Peking Union Medical College, 2A Nan Wei Road, Beijing 100050, China

[4]Department of Chemistry and Applied Biosciences, Institute of Pharmaceutical Sciences, ETH, Zürich, Vladimir-Prelog Weg 4, HCI H405, CH-8093 Zürich, Switzerland

[5]Department of Biological Sciences, Faculty of Science and Engineering, Chuo University, Kasuga, Bunkyo, Tokyo, Japan

[6]Departamento de Ciencias Biomédicas, Unidad Asociada al CSIC por el IQM, Universidad de Alcalá, 28805 Alcalá de Henares, Madrid, Spain

[7]University of Basel, Biozentrum, 4056 Basel, Switzerland

[+]Current address: leadXpro AG, PARK innovAARE, CH-5234 Villigen, Switzerland

[¤]These authors have equally contributed to this work.

[*]Corresponding Authors. fer@cib.csic.es; andrea.prota@psi.ch; wfang@imm.ac.cn

Abstract

Paclitaxel (Taxol®) is a taxane and a first-line chemotherapeutic drug that stabilizes microtubules. While the interaction of paclitaxel with microtubules is well described, the current lack of high-resolution structural information on a tubulin-taxane complex precludes a comprehensive description of the binding determinants that affect the drug's mechanism of action. Here, we solved the crystal structure of the core baccatin III moiety of paclitaxel lacking the C13 side chain in complex with tubulin at 1.9 Å resolution. Based on this information, we engineered two tailor-made taxanes with modified C13 side chains, solved their crystal structures in complex with tubulin, and analyzed their effects along with those of paclitaxel, docetaxel, and baccatin III on the microtubule lattice by X-ray fiber diffraction. We then compared high-resolution structures of ligand-bound tubulin and microtubule complexes with apo forms and used molecular dynamics simulations to understand the consequences of taxane binding to tubulin as well as to simplified protofilament and microtubule-lattice models. Our combined approach sheds light on three mechanistic questions. Firstly, taxanes bind better to microtubules as compared to unassembled tubulin due to a dual structural mechanism: Tubulin assembly is linked to a conformational reorganization of the βM loop, which otherwise occludes ligand access to the taxane site, while the bulky C13 side chains preferentially recognize the microtubule-assembled over the unassembled conformational state of tubulin. Second, the occupancy of the taxane site by a ligand has no influence on the straightness of tubulin protofilaments. Finally, binding of the taxane core to the taxane site displaces the S9-S10 loop of β-tubulin resulting in microtubule expansion. Our results provide detailed new insights into the mechanism of microtubule-stabilization by taxanes.

Introduction

The taxane paclitaxel is a drug included in the World Health Organization's List of Essential Medicines (*1*). Taxanes, either alone or in combination with other chemotherapeutic agents, are important drugs for the treatment of several solid tumors, such as ovarian, lung, and breast cancer, as well as advanced Kaposi's sarcoma (*2-5*). The three taxanes in clinical use, paclitaxel (Taxol®), docetaxel (Taxotere®), and cabazitaxel (Jevtana®), are part of a large family of chemically diverse compounds that bind to the so-called "taxane site" of the αβ-tubulin heterodimer (*6, 7*) (Fig. 1A,B), the building block of microtubules. However, the appearance of peripheral sensory neuropathy and other side effects caused by taxanes compromises treatment efficacy in the long term (*8*). Thus, understanding the underlying mechanism of microtubule stabilization by this class of antitubulin agents is an important requirement for future and safer drug development efforts.

Because taxane-site ligands stabilize microtubules and suppress their dynamics, they are collectively called microtubule-stabilizing agents. Several structures of microtubules in complex with taxane-site agents have been recently analyzed and solved by cryo-electron microscopy to resolutions ranging between ~3 and ~5 Å. For paclitaxel, it was initially suggested that the drug acts on longitudinal tubulin contacts along protofilaments in microtubules by allosterically expanding the microtubule lattice in the direction of its long filament axis (*9-11*), a notion that is also consistent with X-ray fiber diffraction data (*12*). However, more recent studies suggest that paclitaxel enhances lattice flexibility and acts on lateral tubulin contacts between protofilaments in microtubules through interactions with the M-loop of the β-tubulin subunit (βM loop) (*13-15*).

Besides directly acting on microtubules, taxane-site ligands also have the capacity to bind to unassembled tubulin dimers and promote their assembly into microtubules (*16-20*). Several structures of non-taxane agents bound to the taxane-site of tubulin have been solved to resolutions ranging from 2.4 to 1.7 Å by X-ray crystallography (*21-24*). These data suggested that one mode of action of some taxane-site ligands such as zampanolide or epothilone A on unassembled tubulin is to stabilize lateral tubulin contacts between protofilaments within microtubules by structuring and stabilizing the β–tubulin M–loop into a short α-helix (*21*). In contrast, the absence of a helical structure for this segment in the presence of the taxane-site ligands dictyostatin and discodermolide (*22, 23*) suggests

a different, still poorly understood mechanism of microtubule stabilization for these two classes of non-taxane agents.

In the case of taxanes, one hypothesis is that they preferentially bind to a specific conformation of tubulin. It is well established that tubulin displays two prominent conformations that are related to its assembly state (reviewed in (*25*)): a "straight" conformation present in assembled microtubules (denoted "straight tubulin" hereafter) and a "curved" conformation observed in unassembled tubulin (denoted "curved tubulin" hereafter). The "curved-to-straight" conformational transition is required for the formation of lateral tubulin contacts between protofilaments in the main shaft of microtubules. Some data suggest that the activation mechanism of taxanes facilitates the curved-to-straight conformational transition by preferentially binding to the straight conformation of tubulin (*26-28*).

Structural information of a taxane in complex with unassembled tubulin is currently unavailable. With the aim of providing insight into the mechanism of action of this important class of anticancer drugs and into the tubulin-taxane interaction, we solved the high-resolution structures of three different taxanes bound to curved tubulin by X-ray crystallography. We further analyzed the effects of different taxanes on the microtubule lattice by X-ray fiber diffraction. These studies were complemented with molecular dynamics (MD) simulations that shed light on issues that were not amenable to experimental verification. Taken together, our results suggest that the main reason for the differential affinity of taxane-site ligands for assembled tubulin and unassembled tubulin arises from two terms. Firstly, the stabilization of the β M loop in an "out" conformation compatible with the formation of specific lateral contacts in microtubules and secondly, the selectivity of the bulky C13 side chain for the assembled, straight conformational state of tubulin. Finally, we found that the occupancy of the taxane site results in a displacement of the S9-S10 loop of β-tubulin that accounts for the observed microtubule expansion with no influence, however, on the straightness of tubulin protofilaments.

Results

High-resolution crystal structure of a tubulin-taxane complex

To determine the high-resolution structure of a taxane bound to curved tubulin, we performed both soaking and co-crystallization experiments using the previously described protein complexes termed T_2R-TTL and TD1. The former complex is

composed of two αβ-tubulin heterodimers bound head-to-tail, the stathmin-like protein RB3, and the tubulin tyrosine ligase (*21, 29*); the latter complex contains one αβ-tubulin heterodimer and the DARPin D1 (*30*). We did not succeed in procuring any valuable structural information from these two crystal ensembles using a first series of taxanes comprising paclitaxel, docetaxel, the more soluble 3'-*N*-*m*-aminobenzamido-3'-*N*-debenzamidopaclitaxel (N-AB-PT)(*31*), and the engineered, high-affinity taxanes Chitax 40(*32*) and Chitax 68(*33*). We thus decided to approach the issue from a different angle and started off with baccatin III, a precursor in the biosynthesis of paclitaxel that contains both the C2-benzoyloxy ring C and the C10 acetate ester, but lacks the C13 side chain with both the 3'-N-benzamido phenyl ring A and the 3'-phenyl ring B moieties (*34*) (**Fig. 1C**). Notably, baccatin III is largely biologically inactive despite displaying micromolar affinity for microtubules (*35-38*).

We found that baccatin III shows detectable affinity (K_b 25 ºC 3.0±0.5x10^3 M^{-1}) to unassembled tubulin, which is in the same range as for other compounds that have been co-crystallized with tubulin, such as epothilone A 0.8±0.3×10^4 M^{-1} (*39*) and discodermolide 2.0±0.7×10^4 M^{-1} (*40*). Therefore, we hypothesized that the presence of the C13 side chain of the aforementioned taxanes might preclude the binding to the curved tubulin form present in both the T_2R-TTL and the TD1 complexes. Subsequently, we succeeded in obtaining a T_2R-TTL-baccatin III complex structure that was solved at 1.9 Å resolution (**Fig. Sup. 1A,D**; **Table 1**). We found that the ligand binds to the taxane site of curved tubulin with its C2-benzoyloxy ring C stacked between the side chains of βH229 and βL275 in the leucine-rich β-tubulin pocket lined by the side chains of βC213, βL217, βL219, βD226, βH229, βL230 and βL275 (**Fig. 2A**, **3A**). Its carbonyl oxygen forms a weak hydrogen bond to the main chain amide of βR278. The C10 acetate is exposed to the solvent and, together with the C12 methyl, is within van der Waals distance to βG370 of the βS9-βS10 loop. Furthermore, the oxetane oxygen and the C13 hydroxyl accept hydrogen bonds from the main chain amide nitrogen of βT276 and the βH229 imidazole NE2, respectively. The C4 acetate is buried in the hydrophobic pocket made up by βL230, βA233, βF272, βP274, βL275, βM302, βL371, and the aliphatic portion of the βR369 side chain.

Generation of paclitaxel analogs that bind to tubulin crystals

Aiming to understand the implication on tubulin activation of paclitaxel's bulky and hydrophobic C13 ring A moiety (or its equivalent *tert*-butyl in docetaxel) and to elucidate the reason why it apparently precludes binding to T_2R-TTL and TD1 crystals (see above), we devoted a synthetic effort to obtaining new taxane ligands with modified C13 side chains. We produced a series of modified taxanes bearing smaller groups than paclitaxel at the 3'-N position, namely, acrylamide **2a**, haloacetamides **2b** and **2c**, and isothiocyanate **2d** (**Fig. 1C**). We could measure binding of **2a** to unassembled tubulin dimers ($K_{b25°C}$ 0.8±0.3x10^3 M^{-1}), but not of N-AB-PT(*31*), Chitax 40(*32*) or Chitax 68(*33*), thus indicating that the modification of the paclitaxel structure increased the binding affinity for unassembled tubulin. In fact (**Fig. Sup. 1B, C, E, F**), we found unequivocal difference electron densities at the taxane site of β-tubulin in T_2R-TTL crystals soaked with **2a** and **2b** and refined the corresponding structures to 1.95 and 2.35 Å resolution, respectively (**Table 1**).

Interestingly, the electron densities of compounds **2a** and **2b** displayed a continuity between the 3'-N-attached moieties of both ligands and the side chain of βH229 of β-tubulin, suggesting the possible formation of a covalent adduct. For further validation, we collected additional X-ray diffraction data on T_2R-TTL crystals soaked with the haloacetamide derivative **2b** at the bromine peak wavelength of 0.91501 Å. After rigid body and restrained refinement, we detected two clear anomalous difference peaks in electron densities at the taxane sites of the two tubulin dimers in the T_2R-TTL crystals soaked with **2b** (**Fig. Supp. 1F, G**), which did not support covalent bond formation. Furthermore, refinement cycles performed in parallel with **2a** modeled in both the covalent and the non-covalent form, resulted in clear electron density for the non-covalent model, while red difference peaks for the covalent form were always present after refinement (not shown). Accordingly, we interpreted the continuous electron density observed in the T_2R-TTL-**2a** structure as a strong hydrogen bond between the βH229 NE2 and the C39 carbonyl of the ligand side chain rather than a covalent bond (**Fig. 2B**).

The T_2R-TTL-**2a** complex structure revealed that **2a** engages in comparable interactions to curved tubulin by means of both its C2-benzoyloxy ring C and its oxetane moieties, as found for baccatin III (**Fig. 2B, C**). However, the core ring system of **2a** is tilted towards helix βH6 and strand βS7 by ~20˚ (angle between the two C1-C9 axis; $rmsd_{bacIII\text{-}2a}$ of 0.794 Å for 39 core atoms), thereby adopting a pose that is closer to that

observed for paclitaxel bound to straight tubulin in microtubules (PDB ID 6WVR; $rmsd_{2a\text{-}paclitaxel}$ of 0.845 Å for 56 core atoms; $rmsd_{bacIII\text{-}paclitaxel}$ of 1.048 Å for 42 core atoms; **Fig. 3B**).

Similar to paclitaxel bound to straight tubulin, the C39 carbonyl of the C13-3'-N-acrylamide moiety of **2a** forms a hydrogen bond to the βH229 NE2 in curved tubulin (**Figs 2B** and **3B**). The terminal ester moiety of 2a is exposed to the solvent and it forms water-mediated hydrogen bonds to the side chains of βE22 and βR369 of β-tubulin; it lodges within a space that is otherwise occupied by crystallographic water molecules in the curved tubulin-baccatin III structure. In the context of paclitaxel-bound microtubules (straight tubulin), the same space is occupied by the 3'-N-benzamido phenyl ring A of paclitaxel and the side chain of βD26 replaces that of βR369 and adopts a flipped-out conformation (**Figs 2B** and **3B**). The absence of the C10 acetate in **2a** relative to baccatin III has little impact on the conformation of the secondary structural elements shaping the taxane site (**Fig. 2C**).

Together, these structural data provide for the first time a high-resolution structural description of the interaction of taxanes harboring a C13 side chain with unassembled, curved tubulin. They indicate that the main interaction energy of this class of antitubulin agents is mediated by their common baccatin III core moieties. They further reveal that the taxane pose in both curved and straight tubulin is very similar. Overall, our results suggest that the tubulin-**2a** structure is an excellent model to study the interaction of paclitaxel with curved tubulin at high resolution and that X-ray crystallography is a valuable method to analyze the molecular mechanism of action of taxane site microtubule-stabilizing agents.

Conformational changes upon taxane binding to curved and straight tubulin

Next, we investigated the conformational changes induced by binding of baccatin III and **2a** to curved tubulin. To this end, we first superimposed the crystal structures of apo tubulin (PDB ID 4I55), tubulin-baccatin III, and tubulin-**2a** onto the N-terminal β-sheets of β-tubulin (residues 3-9, 63-66, 132-138, 163-169, and 198-202; $rmsd_{BacIII}$ 0.08 Å of 29 C_α; $rmsd_{\mathbf{2a}}$ 0.10 Å of 29 C_α), and calculated the root-mean-square deviations (rmsd) between the apo and the two ligand-bound states. These rmsd values were also

plotted and mapped onto the corresponding structures to highlight the major regions of conformational change.

As shown in **Fig. 4**, significant and comparable conformational changes were observed for backbone atoms of the βT5 loop and the N-terminal segment of the βM loop in both the tubulin-baccatin III and tubulin-**2a** complex structures. Interestingly, the βT5 loop that is prominently involved in establishing longitudinal tubulin contacts along protofilaments is oriented in the active "out" conformation in both structures (*41*). This observation indicates an allosteric crosstalk between the taxane site and the βT5 loop possibly via the central helix βH7 and the guanosine nucleotide bound to β-tubulin. In the case of the βM loop, we only found well-defined electron densities for its N-terminal section up to residue βR278, while the remaining portion of the loop appeared disordered in both complex structures. This partial βM loop structuring has been observed previously in tubulin complexes with the taxane-site ligands dictyostatin and discodermolide ((*22, 23*); note that the taxane-site ligands zampanolide and epothilone A promote the structuring of the βM loop into a helical conformation (*21*)). A direct effect of taxanes on the βM loop is consistent with the notion that paclitaxel stabilizes this secondary structural element in two discrete conformations giving rise to heterogeneous lateral microtubule-lattice contacts (*14*). We also found significant conformational changes in the βS9-βS10 loop, which were more prominent in tubulin-**2a** than in tubulin-baccatin III. This finding can be explained by the presence of a C13 side chain in **2a** that needs more room for accommodation inside the taxane site compared to baccatin III, which lacks a C13 side chain. Finally, we observed a conformational change of the H2' helix in the tubulin-baccatin III structure, which was absent in tubulin-**2a**.

To investigate the effect of the observed conformational changes on the relative domain arrangements in β-tubulin of the individual complexes, we further superimposed the β-tubulin chains of apo tubulin (PDB ID 4I55), tubulin-baccatin III and tubulin-**2a** onto their central βH7 helices (residues 224-243). For tubulin-baccatin III, a subtle relative twist between the N-terminal and the intermediate domains was observed (**Fig. 4**; **Fig. Sup. 2**; **Movies M1 and M2**), while binding of **2a** rather caused both the N-terminal and intermediate domains of β-tubulin to move slightly apart (**Fig. 4**; **Fig. Sup. 2**; **Movies M3 and M4**). Thus, taxane binding to tubulin causes global, but subtle conformational rearrangements.

We next wondered whether similar conformational changes are also observed in straight tubulin in the context of a microtubule upon paclitaxel binding. To this end, we performed the same type of analysis by superimposing the N-terminal β-sheets of β-tubulin from the cryo-EM reconstruction of paclitaxel-bound GDP-microtubules (PDB ID 6WVR) onto the corresponding domains of the undecorated apo GDP-microtubule structure (PDB ID 6DPV; rmsd 0.304 Å 30 C_α). The rmsd analysis revealed similar significant conformational changes of both the βT5 and the βM-loops as observed for the taxanes bound to curved tubulin, however, no prominent perturbations of the βS9-βS10 loop could be detected. In addition, we found significant conformational changes of the βS2'-βS2'' loop (the interacting part of the βM loop with the neighboring protofilament) and the C-terminal βH11-βH12 helix region (**Fig. 3CD**), which were not detected in the curved tubulin structures.

Together, these results suggest that taxane binding in the context of the microtubule should have an effect on the lateral contact established by the βM loop. An effect that cannot be detectable in curved tubulin as this contact does not exist in the crystal. Moreover, we observe an activation effect on the T5-loop, but do not see any direct structural evidence for that, therefore it should be exerted via a crosstalk through the nucleotide.

Effects of taxanes on microtubule lattice parameters

We have previously validated X-ray fiber diffraction of shear-flow aligned microtubules as an accurate technique to determine microtubule lattice parameters (*12, 42*). In such diffraction patterns, the meridional 4-nm layer line is related to the axial helical rise of tubulin monomers in the microtubule lattice. When the lattice is expanded in the direction of the helix axis, a second, weaker 8-nm layer line emerges due to the length difference between the α- and β-tubulin subunits (*42*) and the position of the 1-nm layer line corresponding to the fourth harmonic of the 4-nm layer line moves towards the center of the image.

We used this method to analyze the effect of different conditions on the microtubule lattice (**Fig. 5, Table 2**). We first analyzed microtubules that were assembled in the presence of either GTP (producing GDP-microtubules) or the slowly hydrolyzable GTP analogue GMPCPP (producing GMPCPP-microtubules) and found that the tubulin

dimer rise increased by 0.24 nm (from 8.12±0.02 nm to 8.36±0.02 nm, respectively) in the presence of GMPCPP, a distance that is consistent with that found in previous studies. Concomitantly, the microtubule radius increased from 11.42±0.1 nm for GDP-microtubules to 11.63±0.1 nm for GMPCPP-microtubules, which translates into an increase of the average protofilament number (av. PF nr.) from 12.9 to 13.3, respectively. An increase in both tubulin dimer rise and number of protofilaments for GMPCPP-microtubules compared to GDP-microtubules has been reported previously ((*9, 11, 43, 44*)).

As shown in **Fig. 5** and **Table 2**, and when compared to GDP-bound microtubules, both paclitaxel-bound microtubules and docetaxel-bound microtubules displayed a similar lattice expansion of 0.24 nm as seen for GMPCPP-bound microtubules. Interestingly, while paclitaxel-bound microtubules show a reduced microtubule radius of 10.97±0.1 nm (av. PF nr., 12.21), docetaxel-bound microtubules displayed a radius of 11.53±0.1 nm (av. PF nr., 12.9), which is similar to the value obtained for GDP-microtubules. In the case of paclitaxel, this expansion occurred either when the drug was added before the polymerization reaction was started with GTP- or GDP-tubulin, or when it was added to preformed microtubules, in concordance with rapid structural transitions of microtubules observed upon taxane addition(*45*). Interestingly, microtubules with bound **2a**, **2b** or baccatin III showed similar lattice expansion as those bound to paclitaxel or docetaxel. Note that the diffraction patterns of microtubules stabilized with **2a** or **2b** showed a diffuse 1-nm layer line that reflects variations in the tubulin monomer (and consequently dimer) rise, in clear contrast to those bound by paclitaxel and docetaxel, which displayed a sharp band, i.e., a robust monomer rise.

Taken together, these results suggest that taxanes with or without a C13 side chain have the capacity to expand the microtubule lattice and thus affect longitudinal tubulin contacts along protofilaments. They further indicate that the nature of the C13 side chain can affect the radius of a microtubule and thus lateral tubulin contacts between protofilaments. We note, however, that microtubules assembled in the presence of baccatin III, which lacks a C13 side chain, display the same radius as paclitaxel-bound microtubules. Thus, the presence of a C13 side chain *per se* does not seem to modulate lateral tubulin contacts between protofilaments.

Molecular dynamics simulation analysis of taxane binding to tubulin, protofilament, and microtubule lattice models

Although recent advances in the structural biology of tubulin and microtubules have shed light on the mode of action of taxane-site microtubule stabilizers (*11, 13-15*), there are three main mechanistic questions that remain unsolved. First, previous studies have shown that paclitaxel, docetaxel, epothilone A and discodermolide bind to microtubules with much higher affinities compared to unassembled tubulin (*19, 46, 47*), and that covalent binders like zampanolide react slowly with unassembled tubulin compared to microtubules (*48*). Furthermore, in the present work we have seen that baccatin III and the engineered compounds **2a** and **2b** exhibit sufficient affinity to bind to curved tubulin in T_2R-TTL crystals, while paclitaxel and docetaxel do not. Similarly, the molecular basis accounting for the fact that the affinity for tubulin is two orders of magnitude lower for baccatin III compared to the affinity for microtubules ($3x10^3$ M^{-1} vs $1.5x10^5$ M^{-1} (*38*)) remains also unknown. A second mechanistic question that is unanswered is whether taxanes that bind better to straight tubulin and promote tubulin assembly (i.e., they lower the critical concentration for tubulin assembly (*19, 47*)) are able to induce tubulin straightening upon binding to unassembled tubulin (*27*) or whether they simply provide the necessary free energy by specifically recognizing the microtubule-assembled tubulin form. Finally, we presently lack a molecular rationale explaining the characteristic microtubule-lattice expansion observed upon interaction of taxanes with microtubules (*10-15*).

Although the high-resolution crystallographic structures discussed above provide detailed information of the taxane binding site for the ligands, no large differences were observed between apo and taxane-bound tubulin structures, indicating that additional ligand effects may be related to the dynamic behavior of the protein. For these reasons and to gain further insight into the underlying mechanism of taxane-induced microtubule stabilization, we next used molecular dynamics (MD) simulations to study the behavior of different tubulin assemblies in solution. To this end, we built three types of fully solvated molecular models representing the different oligomerization states of tubulin: (i) the αβ-tubulin heterodimer; (ii) a short protofilament consisting of three longitudinally concatenated tubulin dimers ((αβ-tubulin)$_3$); and (iii) a minimalist representation of a microtubule lattice (*49*) made up of two laterally associated protofilament fragments ((α_1-β_1-α_2)/($\alpha_{1'}$-$\beta_{1'}$-$\alpha_{2'}$)). All models were created in their apo- and taxane-bound forms.

Baccatin III, **2a**, and paclitaxel were chosen as representative taxane ligands for our fully atomistic simulations.

In concordance with the structural results, the MD simulations of the αβ-tubulin heterodimer pointed to the βM loop as the most likely structural element responsible for the selective recognition of the microtubule-assembled tubulin form by taxanes. All taxane-site ligands, including paclitaxel, docetaxel (*19*), discodermolide (*40*), epothilone A (*39*), and **2a** show a loss of affinity of at least four orders of magnitude when binding to unassembled tubulin relative to binding to microtubules. Even baccatin III, which lacks the side chain altogether, has an affinity for the unassembled state that is still two orders of magnitude lower compared to the microtubule-assembled state ($3x10^3$ M^{-1} vs $1.5x10^5$ M^{-1}), a finding that is not explained by our crystallographic data. In our simulations of the tubulin dimer model, we found that the βM loop is the most flexible region (**Fig. S3** top), in good accord with the fact that no density is usually observed for this β-tubulin element in most crystallographic structures. During the course of the MD simulations, this loop was not structured as an α-helix in any of the models studied; instead, it was found to assume a relatively stable, extended hairpin conformation that interacted with and blocked access to the taxane site. Even when the βM loop was initially modeled as an α-helix (as present in all microtubule structures (*11, 13-15*)), this secondary structure element was rapidly lost during the simulated trajectory (**Fig. S3** bottom) regardless of whether or not baccatin III, **2a**, or paclitaxel was bound at the taxane site (**Fig. 6AB**). One likely reason for this behavior is that the bound taxanes do not establish any long-lasting hydrogen-bonding interactions with the amino acids making up this loop (βL275-βL286) so as to stabilize it into an α-helix, as epothilone A and zampanolide do (*21*). Therefore, β-hairpin conformation of the βM loop may compete efficiently with the binding of ligands to the taxane-site (**Movie M5**). As a consequence, the free energy of ligand binding to tubulin dimers with a βM loop partially occluding the taxane site would be expected to be much lower (in the 10^3—10^4 M^{-1} range) than the free energy of binding to microtubules, as is indeed the case (*19, 39, 40*). When considering paclitaxel, entry into the taxane site is further hampered by the fact that this bulky and highly hydrophobic molecule can adopt alternatively collapsed conformations in solution that are different from its bioactive, tubulin-bound T-shape conformation (*50, 51*). The alternative paclitaxel conformations that are inexistent in the case of baccatin III or **2a** further reduce the apparent binding affinity below the solubility limit of the ligand (**Fig. 6C**). These

considerations might explain why we failed to obtain crystal structures of tubulin-paclitaxel and tubulin-docetaxel complexes. Conversely, we think that the laxer binding of the less bulky baccatin III and **2a** molecules compared to paclitaxel (**Fig. S4**) may explain the success in obtaining co-crystal structures with tubulin.

The intermolecular hydrogen bond involving the oxetane O5 and the backbone NH of βT276 is a common feature to all three tubulin-taxane complexes, both in crystals (baccatin III and **2a**) and throughout the simulated MD trajectories (all three ligands). Paclitaxel and **2a** establish two other long-lived hydrogen bonds during our simulations, namely O4':(NE2)βH229 and O2':(O=C)βR369, which may involve ─depending on context─ a βR369-βG370 backbone rearrangement. In turn, the hydroxyl group at C13 of baccatin III alternates between acting as a direct or water-mediated hydrogen bond donor or an acceptor to/from (NE2)βH229 and (O=C)βR369, respectively. In the case of **2a** (and **2b**), on the other hand, it seems that the smaller and more flexible substituents at the C3' position – relative to those present in paclitaxel and docetaxel– allow an adaptation of the βR369-βG370 backbone in the crystal lattice that does not appear to be feasible for the pharmacologically used taxanes.

It has been reported previously that paclitaxel is able to prevent the straight-to-curved conformational transition in GDP-bound microtubules (*27*). However, our simulations indicate that protofilaments are curved both in the absence and in the presence of paclitaxel (**Fig. 6D**), which suggests little or no direct influence of taxanes on the straight-to-curved conformational transition of tubulin. On the other hand, and similar to unassembled tubulin, although in our simulations of the taxane-bound protofilament the occupancy of the taxane site by the ligand constrains the available conformational space of the βM loop compared to that of the apo form, the loop still fails to adopt a well-defined secondary structure in the absence of additional stabilizing interactions with a neighboring protofilament.

Finally, we used a minimalist model of a solvated microtubule lattice in which we could study and compare two taxane-binding sites (β_1 and $\beta_{1'}$), namely, an interfacial one that is highly preorganized for the binding of taxanes due to the stabilization of the βM loop into an α-helix by lateral lattice contacts (site 1), and another one that is fully exposed to the solvent (site 2). We found that the solvent-exposed paclitaxel-bound βM loop is not permanently structured as an α-helix, as expected, and that the major

ligand interactions at site 2 are essentially the same as in the paclitaxel-bound αβ-tubulin heterodimer and the protofilament model (**Fig. S4**). On the other hand, in site 1 dispersion forces, additional H-bonds, the hydrophobic effect, and decreased ligand entropy confer to the studied compounds (paclitaxel, baccatin III, and **2a**) higher binding free energies and longer residence times (i.e., lower k_{off} values) relative to the tubulin dimer and the exposed taxane site 2 (**Fig. S5**). The three H-bond-mediated anchoring points, namely O5:(NH)βT276, O4':(NE2)βH229, and O2':(O=C)βR369, are the same as those observed in the microtubule-paclitaxel complex structure (*13*). The hydrogen bond between the amide carbonyl O4' and the imidazole N^{ε} of βHis229 is maintained in all the **2a** and paclitaxel complexes studied even though this interaction fluctuates substantially, as does the stacking of βHis229 on the benzoyl phenyl ring. However, the most important interaction that is strengthened laterally when a taxane is bound is that involving βTyr283, whose position in the βM loop is fixated by segment ^{85}QIFR^{88} of loop βT3 from the neighboring β-tubulin subunit, as seen previously for other taxane-site ligands like, *e.g.*, zampanolide and taccalonolide AJ (*49*) (**Fig. S5**).

Importantly, our simulations consistently reproduce the axial lattice expansion observed upon paclitaxel binding (*11-13*). We found that the expansion mainly originates from displacement of the βS9-βS10 loop caused by the Φ/Ψ backbone rearrangement in the βR369-βG370 stretch. Because the βS9-βS10 loop acts as a lid covering and stapling the bound taxanes in their final location, this motion propagates toward the attached α-tubulin subunit so that the distance between the α_1- and β_2-tubulin subunits of two longitudinally aligned, consecutive tubulin dimers increases (**Fig. 6E**), a feature that could not be detected in the taxane-bound crystal structures of curved tubulin.

Taken together, these analyses suggest that (i) taxanes bind better to the microtubule-assembled over the unassembled state of tubulin due to the preorganization of the βM loop that otherwise is stabilized in conformations that are incompatible with high-affinity taxane binding; (ii) the bulky C13 side chains preferentially recognize the assembled over the unassembled state of tubulin; (iii) the occupancy of the taxane site has no influence on the straightness of tubulin protofilaments; and (iv) the displacement of the βS9-βS10 loop of β-tubulin by the bound taxane results in microtubule expansion.

Discussion

Previous studies on taxanes left us with several important open issues related to their molecular mechanism of microtubule stabilization. Why do they preferentially bind to the microtubule-assembled over the unassembled tubulin state? Are they involved in structuring of the βM loop, a molecular process that is required for microtubule assembly? Why do they distort/affect the microtubule lattice? Here, we used a combination of ligand engineering, structural biology, and computational approaches to gain insight into these pending questions.

Firstly, we used a rational synthetic approach to dissect which parts of the paclitaxel molecule are involved in particular aspects of tubulin recognition and microtubule stabilization. Our results reveal that paclitaxel's baccatin III core is responsible for filling most of the taxane site and for the key O5:NH(βT276) hydrogen-bonding interaction that is established between taxanes and β-tubulin. However, this interaction has only a marginal effect on the drug's microtubule-stabilizing effect (*35-37*), which requires the C13 side chain to increase the selectivity of the drugs for microtubules over unassembled tubulin. On the other hand, we found that ring A of paclitaxel precludes binding of the drug to the T_2R-TTL and TD1 crystals, while two taxanes with a modified, smaller C13 side chain (**2a** and **2b**) can bind due to the reduced size of their 3'-acylamino substituents and increased flexibility relative to paclitaxel. These smaller substituents allow the newly synthesized taxane derivatives to bind to curved, unassembled tubulin –while keeping their binding poses very similar to that described for paclitaxel when bound to straight tubulin in microtubules– by allowing adaptation of the whole ligand to a rearranged βArg369-βGly370 backbone in the crystal lattice.

Regarding the selective recognition of microtubules by taxanes, we found that it arises from two different terms. The first one is the differential interaction of the bulky C13 side chains with straight and curved tubulin. Our structural analysis reveals that a major structural difference is the environment of the position occupied by the 3'-*N*-benzamido phenyl ring A moiety of paclitaxel in microtubules: in the T_2R-TTL-**2a** structure, the βR369 side chain occupies the same space as the βD26 side chain does in the context of the assembled tubulin conformation in microtubules. The C13 side chain is involved in the interaction with helix βH1 that is flanked by the βH1-βS2. Upon

transition to the microtubule-assembled, straight tubulin state, this space is narrowed down by the side chains of βD26, βK19, βE22, and βH229 to form a favorable environment for the interaction with ring A, which may lock the paclitaxel-bound tubulin in the straight conformation (**Fig. 7B**). In the absence of the C13 side chain (baccatin III) or in the presence of less bulky and "articulated" moieties at the ring A position (**2a** and **2b**; their substituents at the N3 position have a rotatable bond in the middle), ligand binding is likely to be less affected by the curved-to-straight conformational transition, since much looser interactions can still be established with the charged residue side chains of the βS9-βS10 loop and helix H1 through water molecules (**Fig. 2C**, **Fig. 7A**). A second term that accounts for selectivity is occupancy of the taxane site by the βM loop in the absence of lateral contacts, which would be a general mechanism that accounts for the loss of at least four orders of magnitude in affinity when binding to unassembled tubulin relative to microtubules for all taxane-site ligands, including paclitaxel, docetaxel (*19*), discodermolide (*40*), epothilones (*39*), and **2a** (this paper). Our MD simulations of the drug-free tubulin dimer shed new light on why taxanes and other taxane-site ligands bind tubulin dimers with affinities much lower than those reported for microtubules. Whereas in assembled microtubules the βM loop is structured as an α-helix and the preorganized taxane-site is empty and ready to accommodate a ligand, in the unassembled tubulin dimer –as well as in the models of isolated protofilaments and the solvent-exposed site of the minimalist microtubule representation– this same loop displays a large conformational heterogeneity and can adopt a hairpin conformation that allows it to interact with the taxane site and thus to inhibit ligand binding (**Fig. S5**). Moreover, when the tubulin dimer with the βM loop in an α-helical conformation was simulated in complex with baccatin III, **2a**, and paclitaxel, an evolution was systematically observed consisting of βM loop disordering similar to that likely responsible for the lack of electron density in the crystallographic apo structures. The MD analysis indicates that the conformational freedom of the βM loop in unassembled tubulin allows it to occupy the taxane-binding pocket in such a way as to preclude (or compete with) ligand binding. On the other hand, the free energy contribution of taxane-site ligands for microtubule assembly arises from the preferential recognition of the taxane-site conformation present in microtubules (*52*).

Our results point to the βM loop as an essential structural element for the mode of action of paclitaxel and other clinically used taxanes. Our high-resolution structural

analysis of baccatin III in complex with tubulin suggests that even this simplified taxane is able to reduce the flexibility of the βM loop by inducing a partial structuring of its N-terminal region. Further changes occur in the presence of a small C13 side chain, as in **2a** and **2b**, compared to paclitaxel, such as tilting the position of their baccatin III core region by ~20º within the binding pocket and inducing a subtle reorientation of tubulin domains with respect to one another. Despite the fact that we did not observe a complete structuring of the βM loop upon baccatin III, **2a**, or **2b** binding in their respective crystal structures or during MD simulations of free dimers and protofilaments, conformational changes were detected in this β-tubulin region that are in consonance with those observed upon paclitaxel binding to microtubules. Furthermore, our X-ray fiber diffraction studies indicate differences in lateral contacts of shear-flow aligned microtubules bound to baccatin III, **2a**, or **2b**. This observation suggests that paclitaxel and the novel taxanes reported here indeed affect lateral contacts so as to promote microtubule stability through interactions with the N-terminal section of the βM loop, in good agreement with observations reported previously (*14, 15*).

Finally, we found that binding of taxanes to assembled microtubules results in a displacement of the βS9-βS10 loop, which promotes a lattice expansion. The description of the effect of paclitaxel on microtubule lattice parameters has been controversial. Initial analyses suggested that paclitaxel induces lattice expansion (*10, 11*); however, subsequent studies reported only a minor effect (*13-15*). Our present results reinforce the view that lattice expansion is indeed a general consequence of taxane binding and does not require the presence of a C13 side chain. Since baccatin III is essentially biologically inert (*35-38*), our data further indicate that lattice expansion is not an important factor contributing to the mechanism of microtubule stabilization by paclitaxel. Our MD analyses offer a plausible explanation for the taxane-induced longitudinal expansion of microtubules. Although in the complexes with **2a** and **2b** –but not in that with baccatin III–, the crystal structures show that (NH)βG370 hydrogen bonds to the taxane side chain, the simulated complexes indicate that in solution it is the (O=C)βR369 that consistently acts as the hydrogen bond acceptor for the O2' hydroxyl of taxanes. In our view, these findings point to the βS9-βS10 loop as a major structural element that changes on taxane binding, and this change is transmitted to the following α-tubulin subunits on both sides, hence the stretching or longitudinal expansion of the concatenated tubulin dimers. The fact that we observed the Φ/Ψ backbone rearrangement in the βR369-βG370 stretch upon

cooling down the tubulin-paclitaxel complex obtained after the targeted MD procedure (**Movie M7**) points to expansion of the cavity and consolidation of the hydrogen-bonding network as the main factors responsible for this conformational change.

In conclusion, our combined experimental and computational approach allowed us to describe the tubulin-taxane interaction in atomic detail and assess the structural determinants for binding. Our structural analyses further suggest a mode of action of paclitaxel by means of which its core moiety provides the main tubulin-interaction network whilst its C13 side chain enables selective recognition of the prestructured βM loop of the microtubule-assembled tubulin state. Such differential recognition is expected to promote microtubule formation and stabilization. On the other hand, the longitudinal expansion of the microtubule lattices arises from the accommodation of the taxane core within the site, a process that is, however, not related to the microtubule stabilization mechanism of taxanes.

Materials and Methods

Proteins and ligands

Purified calf brain tubulin and chemicals were obtained as previously described(*19, 53*). Paclitaxel (Taxol®) was from Alfa Aesar Chemical, docetaxel (Taxotere®) was kindly provided by Rhône Poulenc Rorer, Aventis (Schiltigheim, France), baccatin III was from Sigma, Flutax-2, Chitax 40, 3'N-aminopaclitaxel (N-AB-PT) and Chitax-68 were synthesized as described(*31-33, 46*). All compounds were diluted in 99.8% DMSO-D6 (Merck) to a final concentration of 20 mM and stored at -20 ºC. Their solubility in aqueous media was determined as described in(*54*), Flutax-2 was found soluble, while a 100 μM solubility was found for docetaxel and a 50 μM for both paclitaxel and Chitax40.

*Synthesis of taxoids **2a-2d**.*

General Experimental Procedures. ^{1}H and ^{13}C NMR spectra were recorded on Varian 400, 500 MHz spectrometers or a Bruker AVANCE III 600 MHz NMR spectrometer. Mass spectra (ESI) was measured on JEOL Accu TOF CS (JMS T100CS). Reagents were purchased from J&K and Alfa Aesar Chemical companies. All anhydrous solvents were purified and dried according to standard procedures, unless otherwise indicated.

Reactions were monitored by TLC (silica gel, GF254) with UV light and H_2SO_4-anisaldehyde spray visualization. The purity of the final compounds was analyzed by HPLC.

7, 10-*O*-di(triethylsilyl)-10-deacetylbaccatin III (4)

To a stirred solution of **3** (1.82 g, 3.3 mmol) in anhydrous tetrahydrofuran (THF) (36 mL) under argon, 4-dimethylaminopyridine (DMAP) (400 mg, 3.3 mmol), triethylamine (TEA) (8.3 mL, 69.4 mmol) and (chlorotriethylsilane) TESCl (4.5 mL, 26.4 mmol) was added dropwise. After the reaction mixture was stirred at room temperature (RT) for 5.5 h, the solution of anhydrous LiBr (291 mg, 3.3 mmol) in anhydrous THF (1.8 mL) was added, the reaction mixture was refluxed at 65-70 °C for 7 h. Once cooled down, the mixture was diluted with ethyl acetate (200 mL). The mixture was washed with saturated aqueous $NaHCO_3$ solution (200 mL) and brine (200 mL), and dried over anhydrous Na_2SO_4. The organic layer was evaporated under reduced pressure. Purification of the crude product by silica gel chromatography (acetone: petroleum ether=1:7) gave 84% yield of product **4** (2.13 g) as a light yellow oil: ^{1}H-NMR (400 MHz, $CDCl_3$): δ 0.55-0.71 p.p.m. (m, 12H), 0.94-1.02 (m, 18H), 1.04 (s, 3H), 1.18 (s, 3H), 1.65 (s, 3H), 1.85-1.91 (m, 1H), 2.01 (s, 3H), 2.22-2.28 (m, 5H), 2.49-2.57 (m, 1H), 3.91 (d, J = 6.8 Hz, 1H), 4.14 (d, J = 8.0 Hz, 1H), 4.27 (d, J = 8.4 Hz, 1H), 4.42 (dd, J = 10.4 Hz, 6.8 Hz, 1H), 4.81 (t, J = 8.0 Hz, 1H), 4.93 (d, J = 8.0 Hz, 1H), 5.21 (s, 1H), 5.61 (d, J = 7.2 Hz, 1H), 7.45 (t, J = 7.6 Hz, 2H), 7.57 (t, J = 7.2 Hz, 1H), 8.09 (d, J = 7.2 Hz, 2H). The ^{1}H NMR data are identical to those for 7, 10-*O*-di(triethylsilyl)-10-deacetylbaccatin III in(*55*).

7,10-*O*-di(triethylsilyl)-2'-*O*-(*tert*-butyldimethylsilyl)-3'-*N*-(de-*tert*-butoxycarbonyl)- 3'-*N*-(benzyloxycarbonyl)docetaxel (6)

A stirred solution of **4** (2.12 g, 2.74 mmol) in anhydrous THF (35.7 mL) under argon was cooled to -45 °C and lithium bis(trimethylsilyl)amide (LHMDS) (0.9 M in methylcyclohexane, 4.6 mL, 4.11 mmol) was added dropwise. The reaction mixture was stirred for 20 min at -45 °C and then, the solution of **5**(*56*) (1.352 g, 3.288 mmol) in anhydrous THF (9 mL) was added and the reaction mixture was stirred for 100 min at the same temperature. Afterwards, the mixture was quenched with saturated aqueous NH_4Cl solution (10 mL) and extracted with ethyl acetate (200 mL*2). The organic layer was washed with saturated aqueous NH_4Cl solution (100 mL) and brine (100 mL), dried over anhydrous Na_2SO_4. Solvent was removed under reduced pressure. Purification of the crude product by silica gel chromatography (acetone: petroleum ether=1:10~1:7) gave

79% yield of product **6** (2.57 g) as a light yellow oil: ^{1}H-NMR (400 MHz, $CDCl_3$): δ -0.31 p.p.m. (s, 3H), -0.08 (s, 3H), 0.56-0.72 (m, 12H), 0.75 (s, 9H), 0.95-1.03 (m, 18H), 1.20 (s, 3H), 1.22 (s, 3H), 1.69 (s, 3H), 1.84 (s, 3H), 1.88-1.96 (m, 2H), 2.33-2.39 (m, 1H), 2.49-2.54 (m, 4H), 3.86 (d, J = 6.8 Hz, 1H), 4.21, 4.29 (ABq, J = 8.4 Hz, each 1H), 4.41 (dd, J = 10.4 Hz, 6.4 Hz, 1H), 4.55 (s, 1H), 4.93 (d, J = 8.4 Hz, 1H), 4.97, 5.02 (ABq, J = 12.4 Hz, each 1H), 5.16 (s, 1H), 5.37 (d, J = 8.8 Hz, 1H), 5.67 (d, J = 7.2 Hz, 1H), 5.72 (d, J = 9.6 Hz, 1H), 6.25 (t, J = 8.4 Hz, 1H), 7.20-7.32 (m, 8H), 7.38 (t, J = 7.2 Hz, 2H), 7.48 (t, J = 7.6 Hz, 2H), 7.57 (t, J = 7.6 Hz, 1H), 8.13 (d, J = 7.2 Hz, 2H); ^{13}C-NMR (150 MHz, $CDCl_3$): δ -6.0, -5.4, 5.3, 5.9, 6.9, 10.5, 13.7, 14.1, 14.2, 18.1, 20.9, 21.0, 22.7, 23.1, 25.4, 26.5, 29.3, 29.6, 29.7, 31.9, 35.6, 37.3, 43.2, 46.6, 57.2, 58.3, 60.3, 66.8, 71.4, 72.6, 75.2, 75.3, 75.5, 76.7, 78.9, 81.2, 84.0, 126.4, 127.7, 127.8, 128.0, 128.4, 128.6, 129.5, 130.2, 133.4, 134.2, 136.3, 137.7, 138.6, 155.7, 167.0, 170.1, 171.1, 171.2, 205.2; ESIMS *m/z* 1184.6 $[M + H]^+$.

7,10-*O*-di(triethylsilyl)-2'-*O*-(*tert*-butyldimethylsilyl)-3'-*N*-(de-*tert*-butoxycarbonyl)docetaxel (7)

To a stirred solution of **6** (2.54 g, 2.14 mmol) in methanol (50 mL), 10% Pd/C (250 mg) was added under H_2 and the reaction mixture was stirred at room temperature for 20 h. The mixture was diluted with methanol (50 mL), filtered and washed with methanol. The organic layer was evaporated under reduced pressure. Purification of the crude product by silica gel chromatography (acetone: petroleum ether=1:8) gave 64% yield of product **7** (1.44 g) as a colorless oil with 18% yield of **6** (0.46 g) recovery: ^{1}H-NMR (500 MHz, DMSO-d_6): δ -0.05 p.p.m. (s, 3H), -0.04 (s, 3H), 0.52-0.62 (m, 12H), 0.84 (s, 9H), 0.90-0.95 (m, 18H), 1.05 (s, 6H), 1.52 (s, 3H), 1.65-1.70 (m, 4H), 1.79-1.84 (m, 1H), 2.02-2.07 (m, 2H), 2.33 (s, 3H), 3.68 (d, J = 7.0 Hz, 1H), 4.02-4.05 (m, 2H), 4.14, 4.30 (ABq, J = 6.0 Hz, each 1H), 4.32 (dd, J = 10.5 Hz, 6.5 Hz, 1H), 4.60 (s, 1H), 4.93 (d, J = 9.5 Hz, 1H), 5.06 (s, 1H), 5.44 (d, J = 7.0 Hz, 1H), 5.89 (t, J = 9.0 Hz, 1H), 7.20-7.22 (m, 1H), 7.35-7.36 (m, 5H), 7.60 (t, J = 7.5 Hz, 2H), 7.70 (t, J = 7.5 Hz, 1H), 7.98 (d, J = 7.0 Hz, 2H); ^{13}C-NMR (125 MHz, DMSO-d_6): δ -5.4, -5.3, 4.8, 5.4, 6.7, 6.8, 10.1, 13.7, 17.9, 20.7, 22.6, 25.5, 26.3, 34.9, 36.8, 42.9, 45.9, 57.7, 58.9, 70.4, 72.4, 74.5, 75.0, 75.5, 76.6, 78.0, 80.0, 83.0, 124.2, 127.3, 128.0, 128.6, 129.5, 130.0, 133.4, 134.2, 137.1, 141.6, 165.2, 169.8, 172.1, 204.7; ESIMS *m/z* 1050.5 $[M + H]^+$.

3'-*N*-(de-*tert*-butoxycarbonyl)-3'-*N*-(4-methoxy-2-methylene-4-oxobutanoyl)docetaxel (2a)

To a stirred solution of **7** (43.6 mg, 0.042 mmol) in anhydrous dichloromethane (DCM) (0.34 mL) under Argon, *N,N'*-Dicyclohexylcarbodiimide (DCC) (17.1 mg, 0.083 mmol), DMAP (2.5 mg, 0.020 mmol) and the solution of itaconic acid monomethyl ester(*57*) (9.2 mg, 0.064 mmol) in DCM (0.15 mL) was added in ice bath. Then, the mixture was stirred for 2 h at room temperature. The mixture was diluted with ethyl acetate (30 mL), filtered by celite and washed with ethyl acetate (30 mL). The organic layer was evaporated under reduced pressure. Purification of the crude product by silica gel chromatography (acetone: hexane=1:9) gave crude product. Subsequently, to a stirred solution of the crude product in acetonitrile (1.7 mL), pyridine (1.0 mL, 12.1 mmol) and HF (0.52 mL, 12.1 mmol) was added and the reaction was stirred at RT for 24 h. Following that, the mixture was diluted with ethyl acetate (50 mL), washed with brine (20 mL), extracted with ethyl acetate (20 mL), and dried over anhydrous Na_2SO_4. The organic layer was evaporated under reduced pressure. Purification of the crude product by silica gel chromatography (acetone: petroleum ether=1:2) gave 32% yield (for two steps) of compound **2a** (11.0 mg) as a white solid: ^{1}H-NMR (600 MHz, CD_3COCD_3): δ 1.11 p.p.m. (s, 3H), 1.20 (s, 3H), 1.69 (s, 3H), 1.80-1.84 (m, 1H), 1.88 (d, J = 1.2 Hz, 3H), 2.16-2.20 (m, 1H), 2.30-2.34 (m, 1H), 2.39-2.45 (m, 4H), 3.34 (s, 2H), 3.61 (s, 3H), 3.89 (d, J = 6.6 Hz, 1H), 4.13, 4.18 (ABq, J = 8.4 Hz, each 1H), 4.25 (dd, J = 11.4 Hz, 6.6 Hz, 1H), 4.69 (d, J = 4.2 Hz, 1H), 4.95 (dd, J = 9.6 Hz, 1.8 Hz, 1H), 5.24 (s, 1H), 5.53 (d, J = 4.2 Hz, 1H), 5.65 (d, J = 7.2 Hz, 1H), 5.73 (d, J = 1.2 Hz, 1H), 6.15-6.18 (m, 2H), 7.27 (t, J = 7.2 Hz, 1H), 7.38 (t, J = 7.8 Hz, 2H), 7.46 (d, J = 7.2 Hz, 2H), 7.54 (t, J = 8.4 Hz, 2H), 7.64 (t, J = 7.2 Hz, 1H), 8.09 (dd, J = 8.4 Hz, 1.2 Hz, 2H); ^{13}C-NMR (150 MHz, CD_3COCD_3): δ 9.1, 13.1, 20.2, 21.7, 25.9, 35.4, 36.1, 38.4, 42.9, 46.1, 51.1, 54.8, 57.2, 70.9, 71.0, 73.2, 73.8, 74.7, 75.6, 77.1, 80.5, 83.9, 126.8, 127.0, 127.5, 127.9, 128.2, 129.6, 129.9, 132.8, 134.6, 136.1, 137.3, 138.9, 165.5, 166.4, 169.3, 170.0, 172.4, 210.1; HRMS (*m/z*): $[M+Na]^+$ calcd for $C_{44}H_{51}NaNO_{15}$, 856.3259; found, 856.3157.

3'-*N*-(de-*tert*-butoxycarbonyl)-3'-*N*-(2-bromoacetyl)docetaxel (2b)

To a stirred solution of **7** (90 mg, 0.086 mmol) in anhydrous DCM (0.9 mL) under Argon, DCC (53.2 mg, 0.26 mmol), DMAP (10.5 mg, 0.086 mmol) and the solution of bromoacetic acid (35.9 mg, 0.26 mmol) in DCM (0.1 mL) was added in ice bath. Then, the mixture was stirred for 2 h at room temperature. The mixture was diluted with ethyl acetate (30 mL), filtered by celite and washed with ethyl acetate (30 mL). The organic

layer was evaporated under reduced pressure. Purification of the crude product by silica gel chromatography (acetone: hexane=1:9) gave crude product (71 mg). Then, a stirred solution of the crude product (54 mg) was solved in 5% HCl/methanol (0.41 mL) in ice bath, and the reaction was stirred in ice bath for 1 h and at room temperature for 12 h. Afterwards, the mixture was diluted with ethyl acetate (50 mL), washed with brine (20 mL), extracted with ethyl acetate (20 mL) and dried over anhydrous Na_2SO_4. The organic layer was evaporated under reduced pressure. Purification of the crude product by silica gel chromatography (acetone: petroleum ether=1:1.5) gave 40% yield (for two steps) of compound **2b** (28.5 mg) as a white solid: ^{1}H-NMR (600 MHz, CD_3COCD_3): δ 1.11 p.p.m. (s, 3H), 1.18 (s, 3H), 1.69 (s, 3H), 1.80-1.84 (m, 1H), 1.88 (d, J = 1.2 Hz, 3H), 2.16-2.20 (m, 1H), 2.29-2.33 (m, 1H), 2.38 (s, 3H), 2.40-2.45 (m, 1H), 3.89 (d, J = 7.2 Hz, 1H), 3.95, 4.00 (ABq, J = 12.0 Hz, each 1H), 4.13, 4.18 (ABq, J = 8.4 Hz, each 1H), 4.23 (dd, J = 11.4 Hz, 6.6 Hz, 1H), 4.70 (d, J = 4.2 Hz, 1H), 4.95 (dd, J = 9.6 Hz, 1.8 Hz, 1H), 5.23 (s, 1H), 5.49 (d, J = 4.2 Hz, 1H), 5.65 (d, J = 7.2 Hz, 1H), 6.16 (t, J = 8.4 Hz, 1H), 7.28 (t, J = 7.2 Hz, 1H), 7.39 (t, J = 7.2 Hz, 2H), 7.47 (d, J = 7.2 Hz, 2H), 7.56 (t, J = 7.8 Hz, 2H), 7.65 (t, J = 7.2 Hz, 1H), 8.09 (d, J = 8.4 Hz, 2H); ^{13}C-NMR (150 MHz, CD_3COCD_3): δ 9.1, 13.1, 20.2, 21.7, 25.8, 35.4, 36.0, 42.8, 46.0, 55.3, 57.2, 59.4, 70.9, 73.0, 73.7, 74.7, 75.6, 77.1, 80.5, 83.8, 126.8, 127.2, 128.0, 128.1, 129.5, 129.9, 132.8, 136.1, 137.2, 138.3, 165.4, 165.9, 170.0, 172.1, 210.0; HRMS (*m/z*): $[M+Na]^+$ calcd for $C_{40}H_{46}NaBrNO_{13}$, 850.2153; found, 850.2037.

3'-*N*-(de-*tert*-butoxycarbonyl)-3'-*N*-(2-iodoacetyl)docetaxel (2c)

Taxoid **2c** was synthesized with iodoacetic acid following the similar procedure for **2b**. Yield of 48% (for two steps), 28.5 mg, white solid: ^{1}H-NMR (600 MHz, CD_3COCD_3): δ 1.12 p.p.m. (s, 3H), 1.19 (s, 3H), 1.71 (s, 3H), 1.80-1.85 (m, 1H), 1.90 (d, J = 1.2 Hz, 3H), 2.22-2.26 (m, 1H), 2.34-2.38 (m, 1H), 2.40 (s, 3H), 2.41-2.46 (m, 1H), 3.82, 3.87 (ABq, J = 9.6 Hz, each 1H), 3.91 (d, J = 7.2 Hz, 1H), 4.14, 4.19 (ABq, J = 8.4 Hz, each 1H), 4.27 (dd, J = 10.8 Hz, 6.6 Hz, 1H), 4.71 (d, J = 3.6 Hz, 1H), 4.95 (dd, J = 9.6 Hz, 2.4 Hz, 1H), 5.23 (s, 1H), 5.51 (d, J = 3.6 Hz, 1H), 5.66 (d, J = 7.2 Hz, 1H), 6.20 (t, J = 9.0 Hz, 1H), 7.29 (t, J = 7.2 Hz, 1H), 7.39 (t, J = 7.2 Hz, 2H), 7.48 (d, J = 7.2 Hz, 2H), 7.56 (t, J = 7.8 Hz, 2H), 7.65 (t, J = 7.8 Hz, 1H), 8.11 (d, J = 9.0 Hz, 1.8 Hz, 2H); ^{13}C-NMR (150 MHz, CD_3COCD_3): δ 9.3, 13.3, 20.4, 21.9, 26.1, 35.6, 36.3, 43.0, 46.3, 55.3, 57.4, 59.6, 71.1, 71.2, 73.2, 74.0, 74.9, 75.8, 77.4, 80.7, 84.0, 127.0, 127.3, 128.2, 128.3, 129.8, 130.1, 133.0, 136.3, 137.4, 138.7, 165.7, 167.7, 170.2, 172.4, 210.2; ESIMS *m/z* 876.2 $[M + H]^+$, 898.2 $[M + Na]^+$.

3'-*N*-(de-*tert*-butoxycarbonyl)-3'-*N*-(2-azidoacetyl)docetaxel (2e)

Taxoid **2e** was synthesized with azidoacetic acid(*58*) following the similar procedure for **2a**. Yield of 83% (for two steps), 25.0 mg, colorless oil: ^{1}H-NMR (500 MHz, CD_3COCD_3): δ 1.12 p.p.m. (s, 3H), 1.18 (s, 3H), 1.69 (s, 3H), 1.79-1.85 (m, 1H), 1.87 (s, 3H), 2.12-2.17 (m, 1H), 2.27-2.32 (m, 1H), 2.36 (s, 3H), 2.40-2.46 (m, 1H), 3.89 (d, J = 7.0 Hz, 1H), 4.01 (s, 2H), 4.13, 4.17 (ABq, J = 8.0 Hz, each 1H), 4.25 (dd, J = 11.0 Hz, 6.5 Hz, 1H), 4.67 (d, J = 4.5 Hz, 1H), 4.95 (d, J = 8.0 Hz, 1H), 5.23 (s, 1H), 5.50 (d, J = 4.5 Hz, 1H), 5.65 (d, J = 7.5 Hz, 1H), 6.16 (t, J = 9.0 Hz, 1H), 7.28 (t, J = 7.5 Hz, 1H), 7.39 (t, J = 7.5 Hz, 2H), 7.47 (d, J = 7.5 Hz, 2H), 7.56 (t, J = 7.5 Hz, 2H), 7.65 (t, J = 7.0 Hz, 1H), 8.09 (d, J = 7.5 Hz, 2H); ^{13}C-NMR (125 MHz, CD_3COCD_3): δ 9.3, 13.3, 20.4, 22.0, 26.0, 35.7, 36.3, 43.0, 46.3, 51.3, 55.4, 57.4, 71.0, 71.2, 73.5, 74.0, 74.9, 75.8, 77.4, 80.7, 84.1, 127.1, 127.5, 128.3, 128.4, 129.8, 130.1, 133.0, 136.4, 137.4, 138.8, 165.6, 167.2, 170.2, 172.4, 210.3; ESIMS *m/z* 813.3 $[M + Na]^+$.

3'-*N*-(de-*tert*-butoxycarbonyl)-3'-*N*-(2-isothiocyanatoacetyl)docetaxel (2d)

To a stirred solution of **2e** (16.4 mg, 0.021 mmol) in anhydrous THF (0.32 mL) under Argon, Ph_3P (8.5 mg, 0.032 mmol) and CS_2 (12.6 μL, 0.21 mmol) were added and the mixture was stirred for 50 h at room temperature. The mixture was evaporated under reduced pressure. Purification of the crude product by silica gel chromatography (acetone: hexane=1:9) gave 83% yield of compound **2d** (28.5 mg) as a white solid: ^{1}H-NMR (600 MHz, CD_3COCD_3): δ 1.08 p.p.m. (s, 3H), 1.10 (s, 3H), 1.67 (s, 3H), 1.76-1.84 (m, 5H), 2.06-2.09 (m, 1H), 2.36 (s, 3H), 2.40-2.45 (m, 1H), 3.85 (d, J = 7.2 Hz, 1H), 4.11, 4.15 (ABq, J = 7.8 Hz, each 1H), 4.18-4.25 (m, 3H), 4.94 (dd, J = 9.6 Hz, 1.8 Hz, 1H), 5.20 (s, 1H), 5.59 (d, J = 7.2 Hz, 1H), 5.65 (d, J = 6.6 Hz, 1H), 6.02 (t, J = 9.0 Hz, 1H), 6.17 (d, J = 10.2 Hz, 1H), 7.25 (t, J = 7.2 Hz, 1H), 7.38 (t, J = 7.8 Hz, 2H), 7.54 (d, J = 7.8 Hz, 2H), 7.61 (t, J = 7.8 Hz, 2H), 7.69 (t, J = 7.8 Hz, 1H), 8.04 (dd, J = 8.4 Hz, 1.2 Hz, 2H); ^{13}C-NMR (150 MHz, CD_3COCD_3): δ 9.0, 13.0, 19.9, 21.7, 25.6, 35.2, 35.9, 42.6, 46.0, 47.4, 57.1, 59.4, 69.7, 69.8, 70.8, 73.6, 74.5, 75.5, 77.0, 80.3, 83.8, 128.0, 128.1, 128.5, 129.4, 129.8, 132.9, 135.5, 136.1, 136.9, 165.3, 169.9, 171.7, 173.3, 209.8; HRMS (*m/z*): $[M+Na]^+$ calcd for $C_{41}H_{46}NaN_2O_{13}S$, 829.2721; found, 829.2619.

Crystallization, Data Collection and Structure Determination

Crystals of T_2R-TTL were generated as described (*21, 29*). Suitable T_2R-TTL crystals were soaked for 8h in reservoir solutions (2-4% PEG 4K, 2-10% glycerol, 30

mM $MgCl_2$, 30 mM $CaCl_2$, 0.1 M MES/Imidazole pH 6.7) containing either 10 mM baccatin III, 5 mM **2a** or **2b.** Subsequently, crystals were flash cooled in liquid nitrogen following a brief transfer into cryo solutions containing the reservoir supplemented with 16% and 20% glycerol. All data were collected at beamline X06DA at the Swiss Light Source (Paul Scherrer Institut, Villigen PSI, Switzerland). Images were indexed and processed using XDS(*59*). Structure solution using the difference Fourier method and refinement were performed using PHENIX(*60*). Model building was carried out iteratively using the Coot software(*61*). Data collection and refinement statistics for all three T_2R-TTL-complexes are given in Table 1. Molecular graphics and analyses were performed with PyMol (The PyMOL Molecular Graphics System, Version 2.3.2, Schrödinger, LLC). To compare the structures of both baccatin III and **2a** complexes in the curved tubulin conformation to the straight tubulin in paclitaxel stabilized microtubule (PDB ID 6WVR), all structures were superimposed onto the taxane-site of **2a** (residues 208-219+225-237+318-320+359-376+272-276+287-296; $rmsd_{BacIII}$ 0.171 Å (48 C_α atoms), $rmsd_{5SYF}$ 0.868 Å (52 C_α atoms)).

Biochemistry

The binding constants of both **2a** and baccatin III to unassembled dimeric tubulin were measured by centrifugation. Increasing amounts of dimeric tubulin (up to 150 μM) prepared in NaPi-GTP buffer (10 mM sodium phosphate, 0.1 mM GTP, pH 7.0) were incubated with a fixed concentration (50 μM) of either baccatin III or **2a**, incubated for 30 min at 25 ºC and centrifuged at 100000 rpm in a TLA-100.2 rotor for 2h at 25 ºC. Then, samples were divided into upper (100 μL) and lower (100 μL) parts and 100 μL of NaPi were added to both of them. Afterwards, 10 μM of either docetaxel or paclitaxel were added as internal standard and samples were subjected three times to an organic extraction using dichloromethane (v:v). Dichloromethane was removed by evaporation and samples were resuspended in methanol 70%. Finally, ligand content was analyzed using an HPLC system (Agilent 1100 Series) and samples were separated using a Zorbax Eclipse XDB-C18 column (Methanol 70% isocratic condition; 20 minutes runs). Tubulin content was determined by BCA for each sample. Ligand concentration in the upper 100 μL was considered as free concentration, while this in the lower 100 μL was considered as the sum of bound and free concentrations. Binding constants of tubulin for the ligand

were calculated assuming a single binding site per tubulin dimer using SIGMAPLOT 14.5 Sigmastat Software Inc.

Microtubule shear-flow alignment and X-ray fiber diffraction experiments

X-ray fiber diffraction data were collected in BL11-NDC-SWEET beamline of ALBA Synchrotron at a λ=0.827 nm as described in(*12*). Radial structural parameters (microtubule diameter and average inter-PT distances) and dimer/monomer length (from the 4th harmonic of the first layer-line signals) were determined as described in(*12*).

Molecular Modeling

In silico model building and molecular dynamics simulations.

Our reduced representation of a straight microtubule (MT) for simulation purposes consisted of the α_1:β_1:α_2 subunits from one protofilament (PF) together with the closely interacting $\alpha_{1'}$:$\beta_{1'}$:$\alpha_{2'}$ subunits from a neighboring PF, as found in the cryo-EM reconstruction of an undecorated MT in complex with zampanolide (PDB code 5SYG, 3.5 Å resolution)(*13*). Likewise, α_1:β_1 made up the isolated dimer, and three concatenated α:β dimers provided the starting straight PF. Missing residues 39-48 in the four α subunits were added, and the partially hydrated Ca^{2+} coordinated by Asp39, Thr41, Gly44, and Glu55 was replaced by Mg^{2+}. Computation of the protonation state of titratable groups at pH 6.8 and addition of hydrogen atoms to each protein ensemble were carried out using the H++ 3.0 Web server (*62*). Nonetheless, in agreement with previous work from our group, the side chain carboxylic group of βGlu200 in the colchicine-binding site was considered to be protonated (*63*) and a disulfide bond was created to link the side chains of βCys241 and βCys356 (*49*). The four guanosine-triphosphate (GTP) and two guanosine-diphosphate (GDP) molecules in the nucleotide-binding sites of α and β tubulin, respectively, were kept, together with their coordinated Mg^{2+} ions and hydrating water molecules. For consistency with the Protein Data Bank, residue numbering and secondary structure assignment herein follow the α-tubulin-based definitions given by Löwe *et al*. (*64*).

The initial molecular models of the taxane complexes were built by best-fit superposition of β-tubulin in their respective crystallographic complexes, as reported here for baccatin and **2a** –and previously for paclitaxel– (*51*), onto the MT, PF or α:β dimer

structure described above. *Ab initio* geometry optimization of baccatin, paclitaxel and **2a**, followed by derivation of atom-centered RESP charges, (*65*) was achieved using a 6-31G* basis set, the Density Functional Tight-Binding (DFTB) method, and the IEF-SCRF continuum solvent model (*66*), as implemented in program Gaussian 09 (Revision D.01)(*67*). The *gaff* (*68*) and *ff14SB* (*69*) AMBER force fields were used for ligand and protein atoms, respectively. The molecular graphics program PyMOL (v. 1.8, Schrödinger LLC) was employed for structure visualization, molecular editing and figure preparation.

All the ligand:tubulin complexes and their respective apo forms were solvated into a cubic box of TIP3P water molecules –with a minimal distance of the protein to the borders of 12 Å– and neutralized by addition of a sufficient number of Na^+ ions. These ensembles were simulated under periodic boundary conditions and electrostatic interactions were computed using the particle mesh Ewald method (*70*) with a grid spacing of 1 Å. The cutoff distance for the non-bonded interactions was 9 Å and the SHAKE algorithm (*71*) was applied to all bonds involving hydrogens so that an integration step of 2.0 fs could be used. All hydrogens and water molecules were first reoriented in the electric field of the solute and then all protein residues, ligands, counterions and waters were relaxed by performing 5 000 steps of steepest descent followed by 50 000 steps of conjugate gradient energy minimization. The resulting geometry-optimized coordinate sets were used as input for the molecular dynamics (MD) simulations at a constant pressure of 1 atm and 300 K using the *pmemd.cuda_SPFP* engine (*72*) as implemented in AMBER 18 for GeForce Nvidia GTX 980 graphics processing units. Ligands, water molecules and counterions were first relaxed around the positionally restrained protein (1 kcal mol^{-1} $Å^{-2}$ on Cα atoms) during a heating and equilibration period lasting 0.5 ns. For the remaining simulation time (from 250 to 1200 ns depending on the system) the macromolecular ensembles were allowed to evolve and coordinates were collected every 0.1 ns for further analysis by means of the *cpptraj* module in AMBER (*73*). Positional restraints were used only in the case of the apo and ligand-bound MT, in which case a weak harmonic restraint (0.5 mol^{-1} $Å^{-2}$) on all Cα atoms (except for those in amino acids 276-374 of both β subunits that make up the βM loops and a large part of the α:β interfaces) was employed to preserve the overall architecture observed in the cryo-EM structure. Snapshots taken every 5 ns were cooled down from 300 to 273 K over a 1-ns period using a simulated annealing procedure (*74*);

the geometries of these "frozen" complexes were then optimized by carrying out an energy minimization until the root-mean-square of the Cartesian elements of the gradient was less than 0.01 kcal·mol^{-1}·Å^{-1}. The resulting ensembles of low-energy and geometrically optimized representative structures, which are expected to be closer to the global energy minima (*49*), were used to calculate the residue-based, solvent-corrected interaction energies.

Geometry and Binding Energy Analysis.

Both the trajectory snapshots and the sets of representative optimized coordinates for each complex studied were analyzed in geometrical terms with the aid of the *cpptraj* routines (*73*) from the AmberTools18 suite. Estimations of the solvent-corrected binding energies were provided by our in-house MM-ISMSA software (*75*), which makes use of a sigmoidal, distance-dependent dielectric function (*76*), and also provides a per-residue decomposition into van der Waals, coulombic, apolar, and desolvation contributions.

Steered MD simulations.

The macromolecular assemblies composed of an α:β dimer in complex with either baccatin or paclitaxel, as obtained after 5 ns of MD equilibration at 300 K, were additionally subjected to a targeted MD dynamics (tMD) procedure by means of which the trajectories were biased so as to force ligand exit firstly and then re-entry into the binding site. The tMD approach was followed essentially as described (*77*) and made use of the parallel implementation of the AMBER *sander.MPI* code running on 4 CPUs, which allows the solvent molecules to move freely and follow the dynamics of ligand and protein. A restraint was defined in terms of a mass-weighted root-mean-square (rms) superposition to the final reference structure (target) that is applied in the force field as an extra energy term of the form $E = 0.5\, k_r\, N\, (rmsd - trmsd)^2$, where k_r is the force constant, N is the number of atoms, and *trmsd* is the target rms deviation. A negative value of the force constant (–0.5 kcal mol^{-1} Å^{-2} over 0.5 ns using only the ligand's oxygen atoms in the rms definition) was employed to force the ligand coordinates away from the initial docking location whereas a positive one was used to find a low-energy path leading from the unbound ligand obtained from the previous procedure back to the initial target structure.

Whereas the same value of 0.5 kcal mol^{-1} Å^{-2} over 0.5 ns proved sufficient to bring baccatin back to its binding pocket, it was considerably more cumbersome to achieve the

same goal in the case of paclitaxel, in which case it was imperative to apply additional conformational restraints to fixate both the T-shape of the ligand and an α-helical βM loop for reasons discussed in the text.

Acknowledgments

We thank Ganadería Fernando Díaz for calf brains supply and staff of beamlines X06DA of the Swiss Light Source (Paul Scherrer Institut, Villigen PSI, Switzerland) and BL11-NDC-SWEET (ALBA, Cerdanyola del Vallès, Spain) for their support. We also thank Mr. Pedro Gascón Blanco for his private donation to the project to support a month of a student salary.

This article is dedicated to the memory of Dr. Linda Amos, a dear friend and pioneer in the study of microtubules and the mechanism of action of paclitaxel(*78*), who passed away while we were assembling this manuscript.

Funding: Ministerio de Ciencia e Innovación PID2019-104545RB-I00 (J.F.D.) and PID2019-104070RB-C22 (F.G.); CSIC PIE 201920E111 (J.F.D.); CSIC PIE 202020E301 (J.F.D.); Proyecto de Investigación en Neurociencia Fundación Tatiana Pérez de Guzmán el Bueno 2020, and by the European Union NextGenerationEU to J.F.D.; EU H2020-MSCA-ITN-2019 860070 TUBINTRAIN (J.F.D. and A.E.P.); Swiss National Science Foundation (310030_192566) (M.O.S.); JSPS KAKENHI (16K07328/17H03668) to (S.K.); NSFC Grant No. 30930108 (W-S. F.); CAMS Innovation Fund for Medical Sciences 2016-I2M-1-010 (W-S.F.).

Author contributions: Conceptualization: A.E.P., K-H.A., W-S.F., M.O.S., and J.F.D.; Investigation: A.E.P., K.B., T.M., F.G., N.O., D.L-A., M.A.O., J.F.D., J. E-G., S.K., Y.M. and S.L.; Visualization: A.E.P., F.G. and M.A.O. Writing of the first draft: A.E.P. and J.F.D. Writing, reviewing, and editing of final manuscript: A.E.P., W-S.F., M.O.S., F.G., M.A.O., and J.F.D.

Competing interests: Authors declare that they have no competing interests.

Data and materials availability: All raw data not presented in the manuscript are available from the authors upon reasonable request: organic synthesis requests should be addressed to W-S. F.; biochemistry and fiber diffraction data requests should be addressed to J.F.D.; crystallographic data requests should be addressed to A.E.P.

Coordinates and structure factors have been deposited at the Protein Data Bank (www.rcsb.org) under accession numbers PDB: 8BDE (T_2R-TTL-**BacIII**), 8BDF (T_2R-TTL-**2a**) and 8BDG ((T_2R-TTL-**2b**).

References

1. *World Health Organization Model List of Essential Medicines – 22nd List, 2021*.
2. D. S. Ettinger, Taxol in the treatment of lung cancer. *J Natl Cancer Inst Monogr*, 177-179 (1993).
3. S. G. Arbuck, A. Dorr, M. A. Friedman, Paclitaxel (Taxol) in Breast Cancer. *Hematology/Oncology Clinics of North America* **8**, 121-140 (1994).
4. M. W. Saville *et al.*, Treatment of HIV-associated Kaposi's sarcoma with paclitaxel. *The Lancet* **346**, 26-28 (1995).
5. K. Lindemann *et al.*, First-line treatment of advanced ovarian cancer with paclitaxel/carboplatin with or without epirubicin (TEC versus TC)—a gynecologic cancer intergroup study of the NSGO, EORTC GCG and NCIC CTG. *Annals of Oncology* **23**, 2613-2619 (2012).
6. J. J. Field, J. F. Diaz, J. H. Miller, The Binding Sites of Microtubule-Stabilizing Agents. *Chemistry & Biology* **20**, 301-315 (2013).
7. M. O. Steinmetz, A. E. Prota, Microtubule-Targeting Agents: Strategies To Hijack the Cytoskeleton. *Trends Cell Biol* **28**, 776-792 (2018).
8. E. Gornstein, T. L. Schwarz, The paradox of paclitaxel neurotoxicity: Mechanisms and unanswered questions. *Neuropharmacology* **76 Pt A**, 175-183 (2014).
9. R. D. Vale, C. M. Coppin, F. Malik, F. J. Kull, R. A. Milligan, Tubulin GTP hydrolysis influences the structure, mechanical properties, and kinesin-driven transport of microtubules. *J Biol Chem* **269**, 23769-23775 (1994).
10. I. Arnal, R. H. Wade, How does taxol stabilize microtubules? *Current Biology* **5**, 900-908 (1995).
11. Gregory M. Alushin *et al.*, High-Resolution Microtubule Structures Reveal the Structural Transitions in αβ-Tubulin upon GTP Hydrolysis. *Cell* **157**, 1117-1129 (2014).
12. J. Estevez-Gallego *et al.*, Structural model for differential cap maturation at growing microtubule ends. *Elife* **9**, (2020).
13. E. H. Kellogg *et al.*, Insights into the Distinct Mechanisms of Action of Taxane and Non-Taxane Microtubule Stabilizers from Cryo-EM Structures. *J Mol Biol* **429**, 633-646 (2017).
14. G. E. Debs, M. Cha, X. Liu, A. R. Huehn, C. V. Sindelar, Dynamic and asymmetric fluctuations in the microtubule wall captured by high-resolution cryoelectron microscopy. *Proceedings of the National Academy of Sciences* **117**, 16976-16984 (2020).
15. S. W. Manka, C. A. Moores, The role of tubulin-tubulin lattice contacts in the mechanism of microtubule dynamic instability. *Nat Struct Mol Biol* **25**, 607-615 (2018).
16. P. B. Schiff, S. B. Horwitz, Taxol assembles tubulin in the absence of exogenous guanosine 5'-triphosphate or microtubule-associated proteins. *Biochemistry* **20**, 3247-3252 (1981).

17. M. F. Carlier, D. Pantaloni, Taxol effect on tubulin polymerization and associated guanosine 5'-triphosphate hydrolysis. *Biochemistry* **22**, 4814-4822 (1983).
18. W. D. Howard, S. N. Timasheff, Linkages between the effects of taxol, colchicine, and GTP on tubulin polymerization. *J Biol Chem* **263**, 1342-1346 (1988).
19. J. F. Díaz, M. Menéndez, J. M. Andreu, Thermodynamics of ligand-induced assembly of tubulin. *Biochemistry* **32**, 10067-10077 (1993).
20. R. M. Buey *et al.*, Interaction of Epothilone Analogs with the Paclitaxel Binding Site; Relationship between Binding Affinity, Microtubule Stabilization, and Cytotoxicity. *Chem Biol* **11**, 225-236 (2004).
21. A. E. Prota *et al.*, Molecular mechanism of action of microtubule-stabilizing anticancer agents. *Science* **339**, 587-590 (2013).
22. C. Trigili *et al.*, Structural Determinants of the Dictyostatin Chemotype for Tubulin Binding Affinity and Antitumor Activity Against Taxane- and Epothilone-Resistant Cancer Cells. *ACS Omega* **1**, 1192-1204 (2016).
23. A. E. Prota *et al.*, Structural Basis of Microtubule Stabilization by Discodermolide. *Chembiochem* **18**, 905-909 (2017).
24. F. A. Balaguer *et al.*, Crystal Structure of the Cyclostreptin-Tubulin Adduct: Implications for Tubulin Activation by Taxane-Site Ligands. *Int J Mol Sci* **20**, (2019).
25. M. Knossow, V. Campanacci, L. A. Khodja, B. Gigant, The Mechanism of Tubulin Assembly into Microtubules: Insights from Structural Studies. *iScience* **23**, 101511 (2020).
26. E. Nogales, S. G. Wolf, K. H. Downing, Structure of the alpha beta tubulin dimer by electron crystallography. *Nature* **391**, 199-203 (1998).
27. C. Elie-Caille *et al.*, Straight GDP-tubulin protofilaments form in the presence of taxol. *Curr Biol* **17**, 1765-1770 (2007).
28. M. P. M. H. Benoit, A. B. Asenjo, H. Sosa, Cryo-EM reveals the structural basis of microtubule depolymerization by kinesin-13s. *Nature Communications* **9**, 1662 (2018).
29. A. E. Prota *et al.*, Structural basis of tubulin tyrosination by tubulin tyrosine ligase. *J Cell Biol* **200**, 259-270 (2013).
30. L. Pecqueur *et al.*, A designed ankyrin repeat protein selected to bind to tubulin caps the microtubule plus end. *Proc Natl Acad Sci U S A* **109**, 12011-12016 (2012).
31. Y. Li, R. Edsall, Jr., P. G. Jagtap, D. G. Kingston, S. Bane, Equilibrium studies of a fluorescent paclitaxel derivative binding to microtubules. *Biochemistry* **39**, 616-623 (2000).
32. R. Matesanz *et al.*, Optimization of taxane binding to microtubules. Binding affinity decomposition and incremental construction of a high-affinity analogue of paclitaxel. *Chem Biol* **15**, 573-585 (2008).
33. Y.-T. Ma *et al.*, A Series of Enthalpically Optimized Docetaxel Analogues Exhibiting Enhanced Antitumor Activity and Water Solubility. *Journal of Natural Products* **81**, 524-533 (2018).
34. G. Samaranayake, K. A. Neidigh, D. G. I. Kingston, Modified Taxols, 8. Deacylation and Reacylation of Baccatin III. *Journal of Natural Products* **56**, 884-898 (1993).
35. J. Parness, D. G. I. Kingston, R. G. Powell, C. Harracksingh, S. B. Horwitz, Structure-activity study of cytotoxicity and microtubule assembly in vitro by taxol and related taxanes. *Biochemical and Biophysical Research Communications* **105**, 1082-1089 (1982).

36. H. Lataste, V. Senilh, M. Wright, D. Guénard, P. Potier, Relationships between the structures of taxol and baccatine III derivatives and their in vitro action on the disassembly of mammalian brain and Physarum amoebal microtubules. *Proceedings of the National Academy of Sciences* **81**, 4090-4094 (1984).
37. D. G. Kingston, Recent advances in the chemistry of taxol. *J Nat Prod* **63**, 726-734 (2000).
38. J. M. Andreu, I. Barasoain, The interaction of baccatin III with the taxol binding site of microtubules determined by a homogeneous assay with fluorescent taxoid. *Biochemistry* **40**, 11975-11984 (2001).
39. A. Canales *et al.*, Molecular recognition of epothilones by microtubules and tubulin dimers revealed by biochemical and NMR approaches. *ACS Chem Biol* **9**, 1033-1043 (2014).
40. A. Canales *et al.*, Insights into the interaction of discodermolide and docetaxel with dimeric tubulin. Mapping the binding sites of microtubule-stabilizing agents using an integrated NMR and computational approach. *ACS Chem. Biol.* **6**, 789-799 (2011).
41. A. Nawrotek, M. Knossow, B. Gigant, The determinants that govern microtubule assembly from the atomic structure of GTP-tubulin. *J Mol Biol* **412**, 35-42 (2011).
42. S. Kamimura, Y. Fujita, Y. Wada, T. Yagi, H. Iwamoto, X-ray fiber diffraction analysis shows dynamic changes in axial tubulin repeats in native microtubules depending on paclitaxel content, temperature and GTP-hydrolysis. *Cytoskeleton* **73**, 131-144 (2016).
43. A. A. Hyman, S. Salser, D. N. Drechsel, N. Unwin, T. J. Mitchison, Role of GTP hydrolysis in microtubule dynamics: information from a slowly hydrolyzable analogue, GMPCPP. *Mol Biol Cell* **3**, 1155-1167 (1992).
44. H. Yajima *et al.*, Conformational changes in tubulin in GMPCPP and GDP-taxol microtubules observed by cryoelectron microscopy. *The Journal of cell biology* **198**, 315-322 (2012).
45. J. F. Díaz, J. M. Valpuesta, P. Chacón, G. Diakun, J. M. Andreu, Changes in microtubule protofilament number induced by Taxol binding to an easily accessible site. Internal microtubule dynamics. *J Biol Chem* **273**, 33803-33810 (1998).
46. J. F. Diaz, R. Strobe, Y. Engelborghs, A. A. Souto, J. M. Andreu, Molecular recognition of taxol by microtubules. Kinetics and thermodynamics of binding of fluorescent taxol derivatives to an exposed site. *J Biol Chem* **275**, 26265-26276 (2000).
47. R. M. Buey *et al.*, Microtubule interactions with chemically diverse stabilizing agents: Thermodynamics of binding to the paclitaxel site predicts cytotoxicity. *Chem. Biol.* **12**, 1269-1279 (2005).
48. J. J. Field *et al.*, Zampanolide, a potent new microtubule-stabilizing agent, covalently reacts with the taxane luminal site in tubulin alpha,beta-heterodimers and microtubules. *Chem Biol* **19**, 686-698 (2012).
49. P. A. Sánchez-Murcia, A. Mills, Á. Cortés-Cabrera, F. Gago, Unravelling the covalent binding of zampanolide and taccalonolide AJ to a minimalist representation of a human microtubule. *Journal of computer-aided molecular design* **33**, 627-644 (2019).
50. J. P. Snyder, J. H. Nettles, B. Cornett, K. H. Downing, E. Nogales, The binding conformation of Taxol in beta-tubulin: A model based on electron crystallographic density. *Proc Natl Acad Sci U S A* **98**, 5312-5316 (2001).

51. C. Coderch *et al.*, A structure-based design of new C2- and C13-substituted taxanes: tubulin binding affinities and extended quantitative structure-activity relationships using comparative binding energy (COMBINE) analysis. *Org Biomol Chem* **11**, 3046-3056 (2013).
52. E. Nogales, M. Whittaker, R. A. Milligan, K. H. Downing, High-resolution model of the microtubule. *Cell* **96**, 79-88 (1999).
53. J. M. Andreu, in *Microtubule Protocols,* J. Zhou, Ed. (Humana Press, Totowa, NJ, 2007), pp. 17-28.
54. G. Saez-Calvo *et al.*, Triazolopyrimidines Are Microtubule-Stabilizing Agents that Bind the Vinca Inhibitor Site of Tubulin. *Cell Chem Biol* **24**, 737-750 e736 (2017).
55. L.-R. Kung *et al.* (2012).
56. I. Ojima *et al.*, A New Paclitaxel Photoaffinity Analog with a 3-(4-Benzoylphenyl)propanoyl Probe for Characterization of Drug-Binding Sites on Tubulin and P-Glycoprotein. *J. Med. Chem.* **38**, 3891-3894 (1995).
57. R. N. Ram, N. K. Meher, A Simple Method for the Preparation of Monomethyl Esters of Dicarboxylic Acids by Selective Esterification of the Nonconjugated Carboxyl Group in the Presence of an Aromatic or Conjugated Carboxyl Group. *J. Chem. Res. (S)* **2000**, 282-283 (2000).
58. N. Brabez *et al.*, Design, Synthesis, and Biological Studies of Efficient Multivalent Melanotropin Ligands: Tools toward Melanoma Diagnosis and Treatment. *J. Med. Chem.* **54**, 7375-7384 (2011).
59. W. Kabsch, XDS. *Acta Crystallogr. Sect. D* **66**, 125-132 (2010).
60. P. D. Adams *et al.*, PHENIX: a Comprehensive Python-based System for Macromolecular Structure Solution. *Acta Crystallogr. Sect. D* **66**, 213-221 (2010).
61. P. Emsley, B. Lohkamp, W. G. Scott, K. Cowtan, Features and development of Coot. *Acta Crystallogr D Biol Crystallogr* **66**, 486-501 (2010).
62. R. Anandakrishnan, B. Aguilar, A. V. Onufriev, H++ 3.0: automating pK prediction and the preparation of biomolecular structures for atomistic molecular modeling and simulations. *Nucleic Acids Res* **40**, W537-541 (2012).
63. O. Bueno *et al.*, High-affinity ligands of the colchicine domain in tubulin based on a structure-guided design. *Sci Rep* **8**, 4242 (2018).
64. J. Löwe, H. Li, K. H. Downing, E. Nogales, Refined structure of alpha beta-tubulin at 3.5 A resolution. *J Mol Biol* **313**, 1045-1057 (2001).
65. J. Wang, P. Cieplak, P. A. Kollman, How well does a restrained electrostatic potential (RESP) model perform in calculating conformational energies of organic and biological molecules? *Journal of Computational Chemistry* **21**, 1049-1074 (2000).
66. G. Scalmani, M. J. Frisch, Continuous surface charge polarizable continuum models of solvation. I. General formalism. *J Chem Phys* **132**, 114110 (2010).
67. Gaussian 09 M. J. Frisch *et al.* (2009).
68. J. Wang, R. M. Wolf, J. W. Caldwell, P. A. Kollman, D. A. Case, Development and testing of a general amber force field. *J Comput Chem* **25**, 1157-1174 (2004).
69. J. A. Maier *et al.*, ff14SB: Improving the Accuracy of Protein Side Chain and Backbone Parameters from ff99SB. *Journal of Chemical Theory and Computation* **11**, 3696-3713 (2015).
70. R. Salomon-Ferrer, A. W. Götz, D. Poole, S. Le Grand, R. C. Walker, Routine Microsecond Molecular Dynamics Simulations with AMBER on GPUs. 2.

Explicit Solvent Particle Mesh Ewald. *Journal of Chemical Theory and Computation* **9**, 3878-3888 (2013).

71. J.-P. Ryckaert, G. Ciccotti, H. J. C. Berendsen, Numerical integration of the cartesian equations of motion of a system with constraints: molecular dynamics of n-alkanes. *Journal of Computational Physics* **23**, 327-341 (1977).
72. S. Le Grand, A. W. Götz, R. C. Walker, SPFP: Speed without compromise—A mixed precision model for GPU accelerated molecular dynamics simulations. *Computer Physics Communications* **184**, 374-380 (2013).
73. D. R. Roe, T. E. Cheatham, PTRAJ and CPPTRAJ: Software for Processing and Analysis of Molecular Dynamics Trajectory Data. *Journal of Chemical Theory and Computation* **9**, 3084-3095 (2013).
74. A. T. Brunger, P. D. Adams, Molecular Dynamics Applied to X-ray Structure Refinement. *Accounts of Chemical Research* **35**, 404-412 (2002).
75. J. Klett *et al.*, MM-ISMSA: An Ultrafast and Accurate Scoring Function for Protein–Protein Docking. *Journal of Chemical Theory and Computation* **8**, 3395-3408 (2012).
76. A. Morreale, R. Gil-Redondo, A. R. Ortiz, A new implicit solvent model for protein-ligand docking. *Proteins* **67**, 606-616 (2007).
77. F. Rodríguez-Barrios, J. Balzarini, F. Gago, The Molecular Basis of Resilience to the Effect of the Lys103Asn Mutation in Non-Nucleoside HIV-1 Reverse Transcriptase Inhibitors Studied by Targeted Molecular Dynamics Simulations. *Journal of the American Chemical Society* **127**, 7570-7578 (2005).
78. L. A. Amos, J. Lowe, How Taxol stabilises microtubule structure. *Chem Biol* **6**, R65-69 (1999).

Figures and Tables

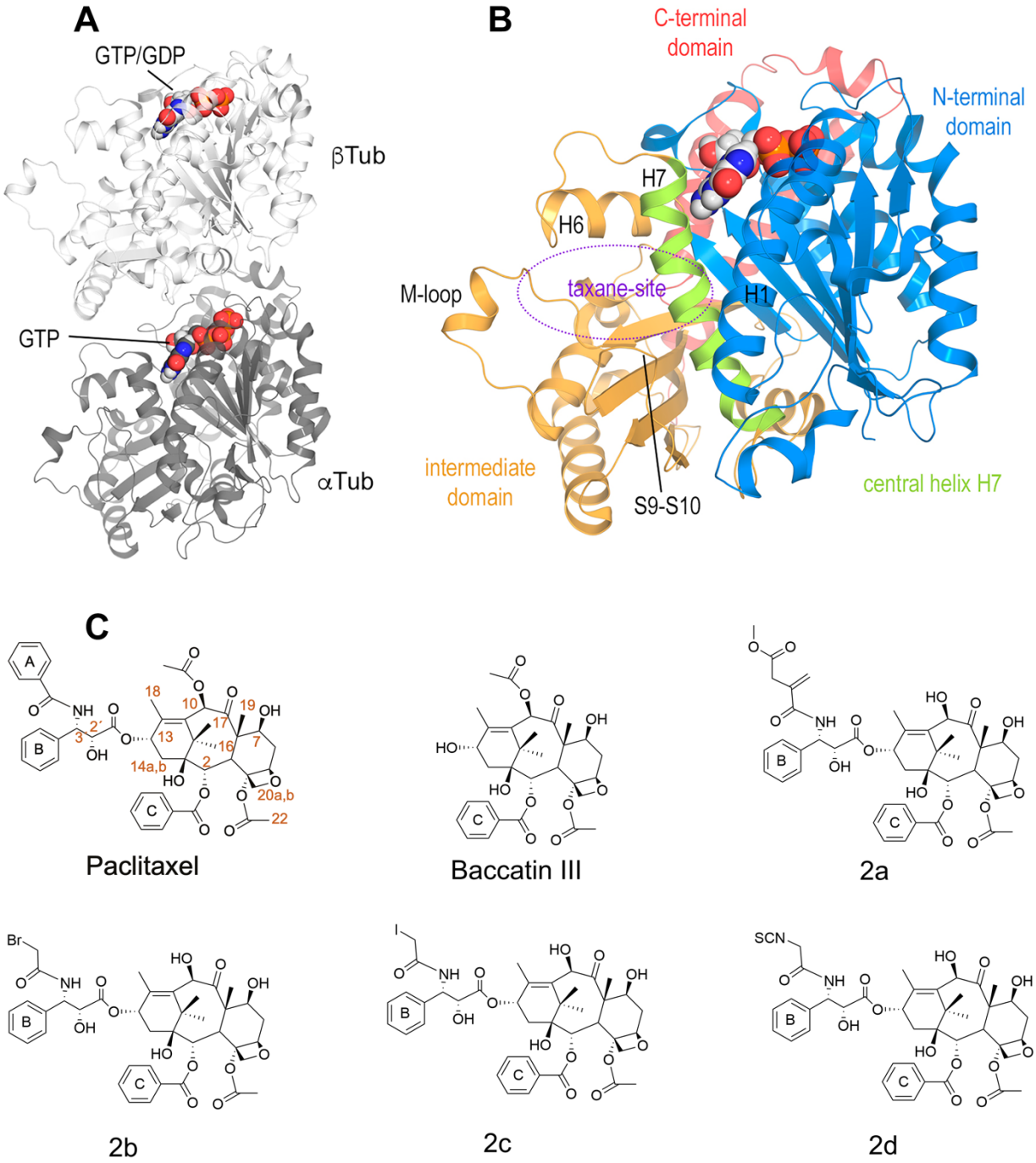

Figure 1. (**A**) Tubulin heterodimer (α-tubulin in gray and β-tubulin in white) in ribbon representation, where nucleotide binding sites have been highlighted in sphere representation **(B)** Structural features of the tubulin β-subunit. (**C**) Structures of taxanes used in this study.

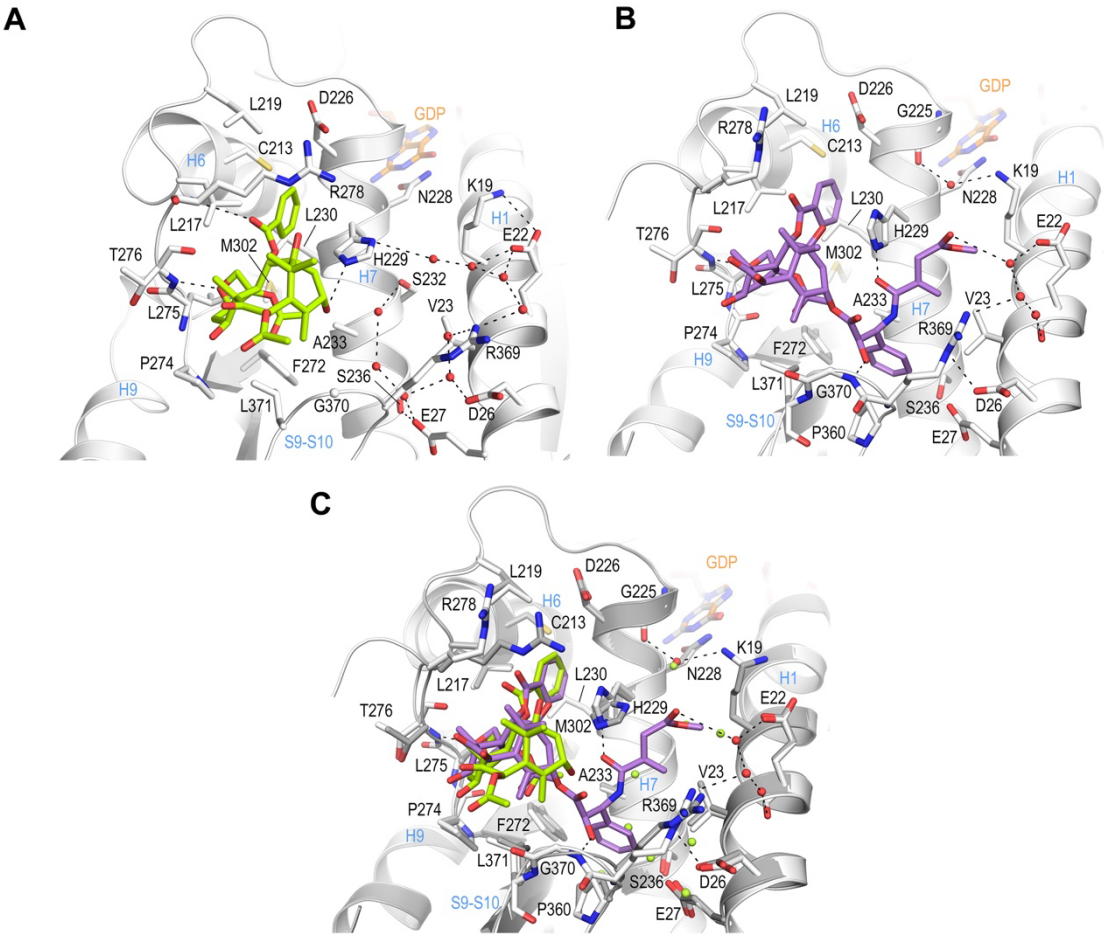

Figure 2. Crystal structure of T_2R-TTL-baccatin III and T_2R-TTL-2a complexes. (**A**) Close-up view of the interaction network observed between baccatin III (lemon) and β-tubulin (light gray). Interacting residues of tubulin are shown in stick representation and are labeled. Oxygen and nitrogen atoms are colored red and blue, respectively; carbon atoms are in lemon (baccatin III) or light gray (tubulin). Hydrogen bonds are depicted as black dashed lines. Secondary structural elements of tubulin are labeled in blue. (**B**) Close-up view of the interaction of **2a** (violet) with β-tubulin in the same view and representation as in (**A**). (**C**) The same close-up view as in (**A**) and (**B**) with the superimposed baccatin III (lemon) and **2a** (violet) complex structures. Water molecules belonging to the baccatin III structure are represented as lemon spheres.

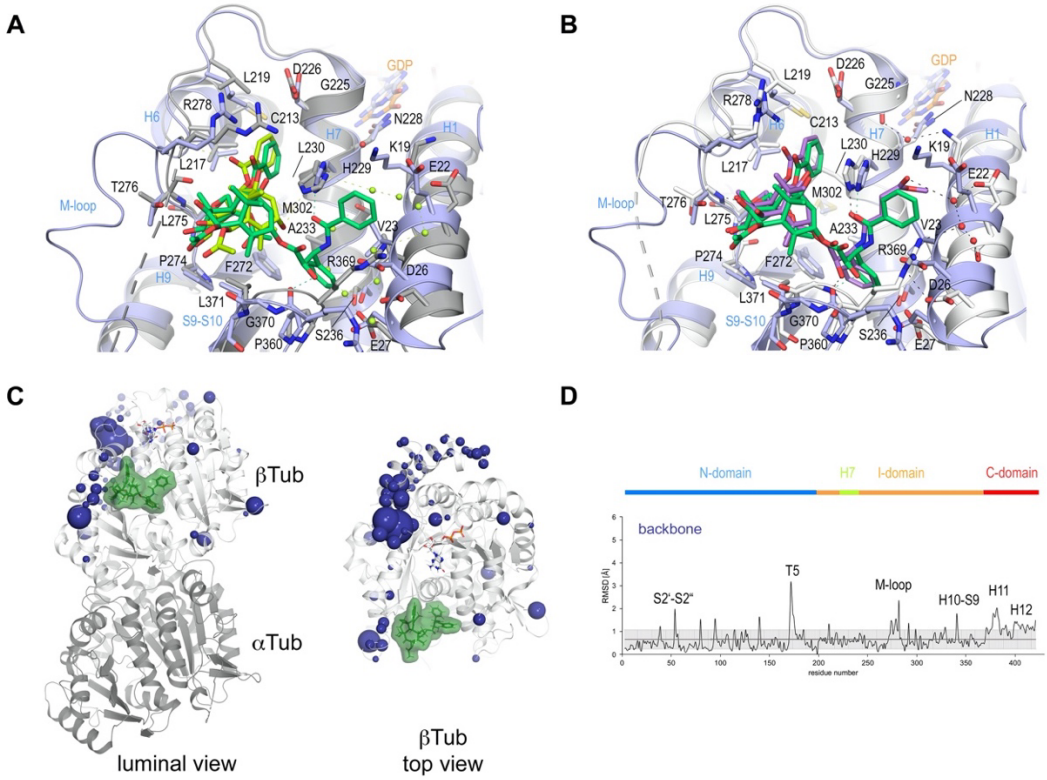

Figure 3. Comparison of taxane binding to unassembled curved versus assembled straight tubulin. (**A**) Close-up view of the superimposed baccatin III bound (ligand in lemon; protein in grey ribbon and sticks) to curved tubulin and paclitaxel bound to straight tubulin as found in a microtubule (PDB ID 6WVR; ligand in dark green; protein in slate ribbon and sticks) structures. Interacting residues of tubulin are shown in stick representation and are labeled. Oxygen and nitrogen atoms are colored red and blue, respectively. Hydrogen bonds are depicted as black dashed lines. Secondary structural elements of tubulin are labeled in blue. Water molecules belonging to the baccatin III structure are represented as lemon spheres. The structures were superimposed onto their taxane-sites (residues 208–219 + 225–237 + 272–276 + 286–296 + 318–320 + 359–376; rmsd 0.894 Å (52 C_α atoms). (**B**) Close-up view of superimposed **2a** bound to curved tubulin (ligand in violet; protein in grey ribbon and sticks) and paclitaxel bound to straight tubulin (PDB ID 6WVR; ligand in dark green; protein in slate ribbon and sticks) structures (rmsd 0.826 Å over 52 C_α atoms) using the same settings as in (**A**). (**C**) Conformational changes on β-tubulin induced by paclitaxel upon binding to straight tubulin in microtubules (PDB ID 6WVR). The α-tubulin and β-tubulin chains are in ribbon representation and are colored in dark and light grey, respectively. The rmsd differences between unbound and paclitaxel-bound straight tubulin are represented as dark (backbone rmsd) blue spheres. Only the rmsd-differences above a threshold of average ± standard deviation are displayed. The sphere-radii correspond to the average-subtracted rmsd-values displayed in panel (**D**). (**D**) Rmsd plots of backbone positions between the paclitaxel bound (PDB ID 6WVR) and the apo (PDB ID 6DPV) straight tubulin in microtubules. The grey error bar represents the average rmsd ± standard deviation. The top bar is colored according to the following domain assignment: N-terminal domain (N-domain., marine blue), intermediate domain (I-domain, orange), central helix βH7 (lemon) and C-terminal domain (C-domain, red). The β-tubulin chains of the corresponding structures were superimposed onto their β-tubulin N-terminal β-sheets (rmsd 0.304 Å over 30 C_α).

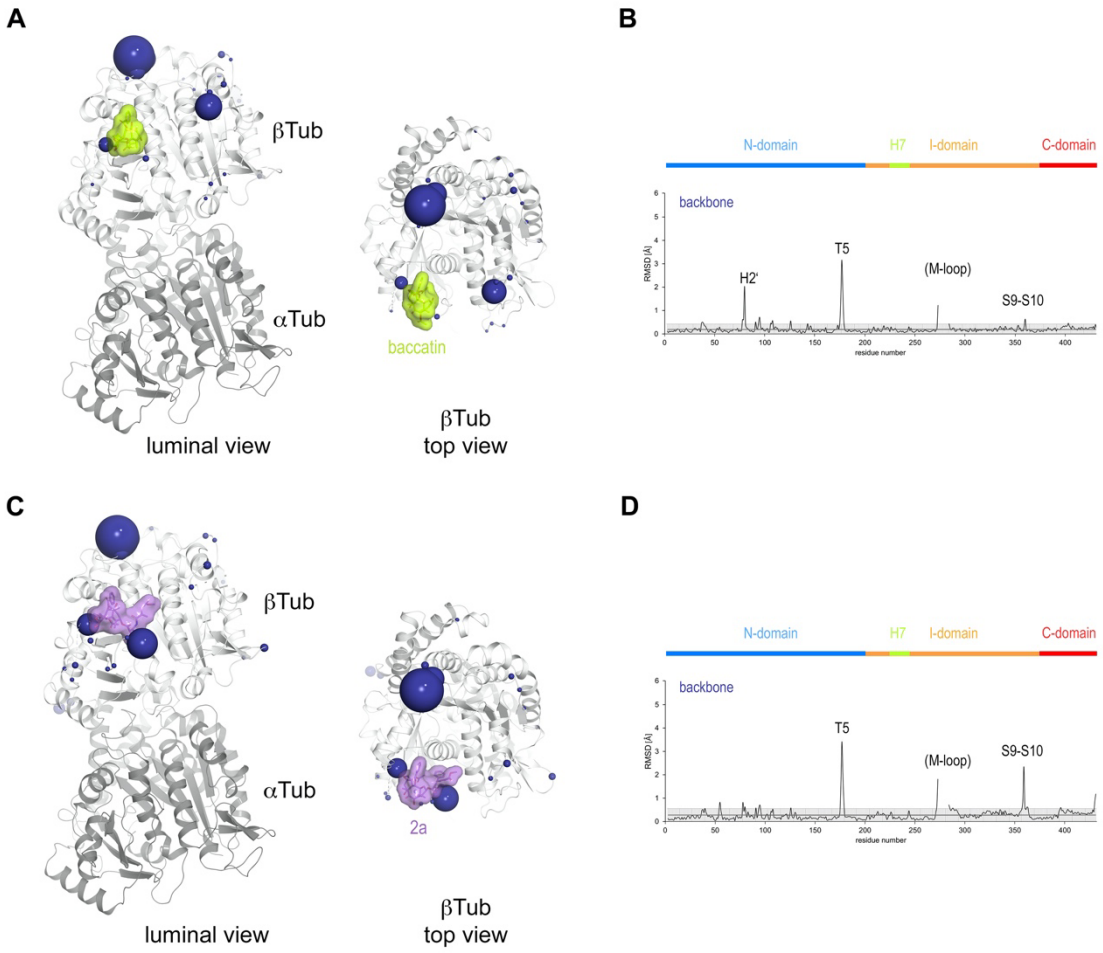

Figure 4. Conformational changes induced by taxane binding to unassembled, curved tubulin. (**A**) Conformational changes on the backbone atoms (dark blue) of the β-tubulin chain induced by baccatin III upon binding to curved tubulin. The tubulin chains are in ribbon representation and are colored in dark (α-tubulin) and light (β-tubulin) grey, respectively. The rmsd-values of the superimposed unbound and baccatin III bound curved tubulin are represented as dark blue (backbone rmsd) spheres, respectively. Only the rmsd-values above a threshold of average + standard deviation are displayed. The sphere-radii correspond to the average-subtracted rmsd-values displayed in panel (**B**). (**B**) Rmsd plots of the backbone (bottom) positions between the baccatin bound and the apo (PDB ID 4I55) curved tubulin state. The grey error bar represents the average rmsd ± standard deviation. The top bar is colored according to the following domain assignment: N-terminal domain (N-domain, marine blue), intermediate domain (I-domain, orange), central helix H7 (lemon), C-terminal domain (C-domain, red). The β-tubulin chains of the corresponding structures were superimposed onto their β-tubulin N-terminal β-sheet (rmsd 0.08 Å over 29 C_α). (**C**) Conformational changes on the backbone atoms (dark blue) of the β-tubulin chain induced by **2a** upon binding to curved tubulin. (**D**) Rmsd plots of the backbone (bottom) positions between the **2a** bound and the apo (PDB ID 4I55) curved tubulin state (rmsd 0.10 Å over 29 C_α). The same display settings as in (**B**) are applied.

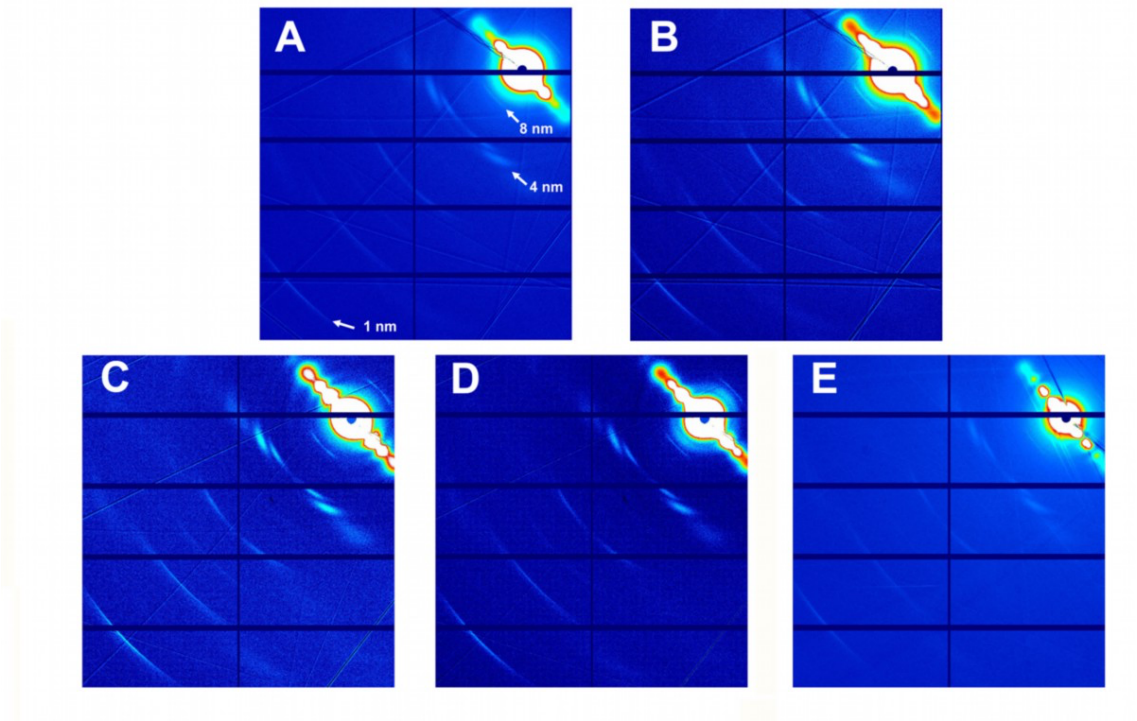

Figure 5.- Fiber diffraction patterns of microtubules. Microtubules assembled from GTP-tubulin and paclitaxel (**A**), GTP-tubulin and docetaxel (**B**), GTP-tubulin and **2a** (**C**), GTP-tubulin and **2b** (**D**), and GTP-tubulin and baccatin III (**E**) are shown.

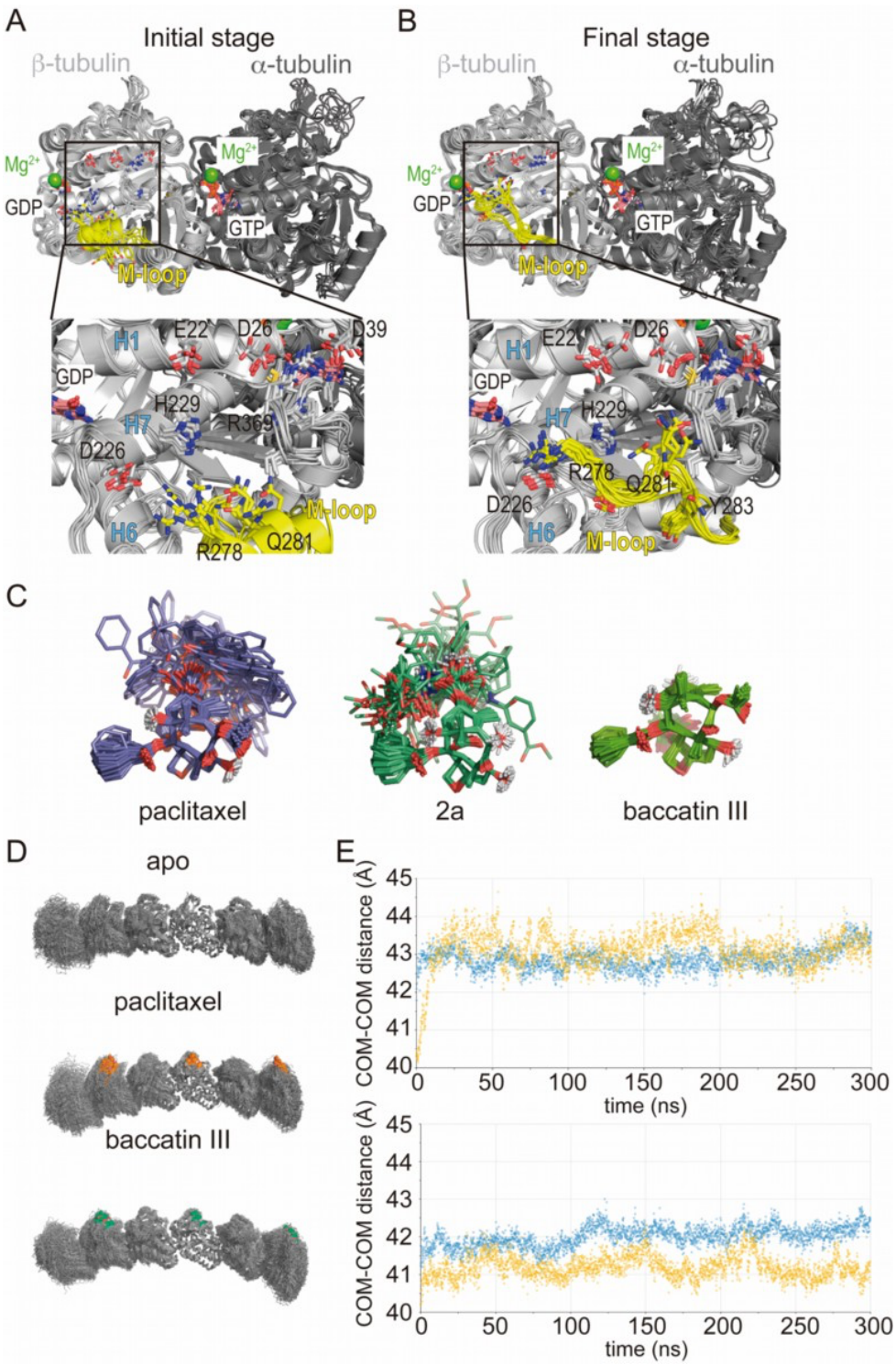

Figure 6.- **Molecular dynamics simulation of tubulin-taxane complexes. (A,B)** MD simulation of the free αβ-tubulin dimer. **(A)** Initial stage of the simulation, starting from a βM loop (residues β275-β286; yellow) organized as a α-helix akin to what is observed in a microtubule and **(B)** after 100 ns of a MD simulation. **(C)** Overlaid snapshots taken every 5 ns over the course of a 250-ns MD simulation of paclitaxel (left), **2a** (middle), or baccatin III (right). **(D)** Snapshots of the protofilament model bound to paclitaxel or baccatin III and apo form. **(E)** Time evolution of the intermonomer distances (measured between the respective centers of mass; α2-β2 in blue and β2-α3 in yellow) in the simulated apo and liganded protofilaments.

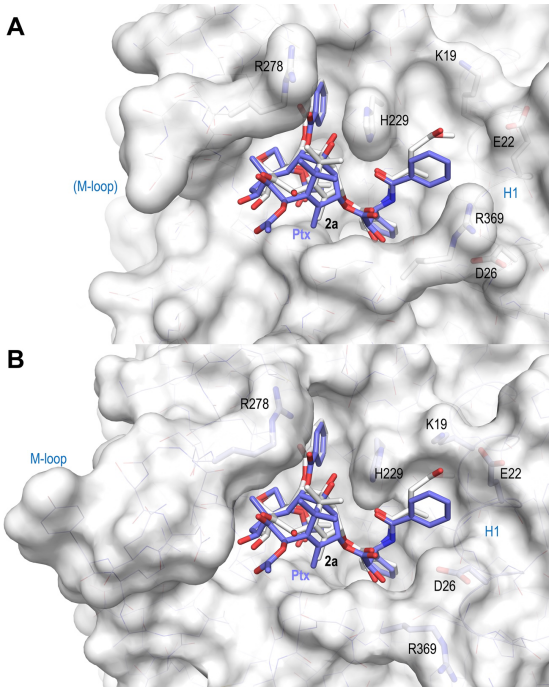

Figure 7. Surface representations of liganded taxane sites in both the curved and straight tubulin conformational states. (A) Curved tubulin; (B) straight tubulin. The structures of **2a** (white) and paclitaxel (slate) bound to microtubules (PDB ID 6WVR) were superimposed onto their central helices βH7. The side chains of the βM loop residue βR278 and of residues surrounding the C13 side chains of the ligands are in stick representation and are labeled. Helix βH1 is highlighted in ribbon representation.

Table 1 X-ray data collection and refinement statistics

	T_2R-TTL-BacIII	T_2R-TTL-**2a**	T_2R-TTL-**2b**
Data collection			
Space group	$P2_12_12_1$	$P2_12_12_1$	$P2_12_12_1$
Cell dimensions			
a, *b*, *c* (Å)	104.1, 157.2, 179.2	104.8, 157.9, 179.1	105.3, 158.6, 179.2
Resolution (Å)	49.2-1.9 (1.95-1.90)	49.3-1.95 (2.00-1.95)	49.4-2.35 (2.41-2.35)
R_{merge}*(%)*	10.7 (491.9)	13.3 (516.6)	17.4 (403.5)
R_{meas} *(%)*	11.1 (513.1)	13.6 (526.1)	17.7 (410.8)
R_{pim} *(%)*	3.3 (147.5)	2.9 (102.9)	2.6 (57.7)
I / σI	16.5 (0.5)	20.1 (0.7)	20.1 (0.9)
CC half	100 (17.8)	100 (31.4)	99.9 (46.6)
Completeness (%)	100 (99.8)	100 (100)	100 (100)
Redundancy	13.5 (12.4)	27.3 (27.8)	28.5 (28.3)
Refinement			
Resolution (Å)	49.2-1.9	49.3-1.95	49.4-2.35
No. unique reflections	229654	215774	125168
R_{work} / R_{free}	19.2 / 21.8	18.9 / 21.6	18.3 / 21.4
No. atoms			
Protein	17555	17389	17227
Ligand	42	120	
Water	861	883	166
Average *B*-factors (Å^2)			
Protein	59.0	62.9	76.1
Ligand (chain B / D)	n.a. / 109.2	111.4 / 102.8	146.6 / 144.9
Water	56.2	60.3	59.4
Wilson *B*-factor	41.7	43.1	56.9
R.m.s. deviations			
Bond lengths (Å)	0.003	0.003	0.002
Bond angles (°)	0.642	0.655	0.550
Ramachandran statistics			
Favored regions (%)	98.1	98.1	98.0
Allowed regions (%)	1.8	1.8	2.0
Outliers (%)	0.1	0.1	0

*For each structure, data were collected from a single crystal. *Values in parentheses are for highest-resolution shell.

1226 **Table 2. Structural parameters of microtubules assembled in the presence of different nucleotides and drugs*.**

	paclitaxel-Pre microtubules	paclitaxel- Post microtubules	paclitaxel-GDP Tubulin	GDP-microtubules	GMPCPP-microtubules	Docetaxel-microtubules	Baccatin III -microtubules	2a-microtubules	2b-microtubules
microtubule radius (nm)	10.97±0.10	11.04±0.51	10.98±0.47	11.42±0.10	11.63±0.10	11.53±0.10	11.06±0.35	11.27±0.57	11.60±0.36
Avg. PF number	12.21±0.10	12.28±0.71	12.23±0.65	12.91±0.10	13.29±0.10	12.90±0.10	12.29±0.39	12.63±0.72	12.99±0.40
Inter-PF distances (nm)	5.58±0.01	5.59±0.33	5.57±0.29	5.50±0.03	5.45±0.03	5.57±0.01	5.61±0.18	5.55±0.31	5.56±0.17
Avg. monomer length (nm)	4.18±0.01	4.18±0.01	4.18±0.01	4.06±0.01	4.18±0.010	4.18±0.01	4.16±0.03	4.15±0.03	4.13±0.03
1 nm band peak position (nm^{-1})	6.02±0.01	6.02±0.01	6.02±0.01	6.19±0.01	6.02±0.01	6.02±0.01	6.04±0.5	6.06±0.05	6.08±0.05
8 nm band	Yes	Yes	Yes	No	Yes	Yes	Yes	Yes	Yes

1227

1228 *Errors are SE of three independent

1229

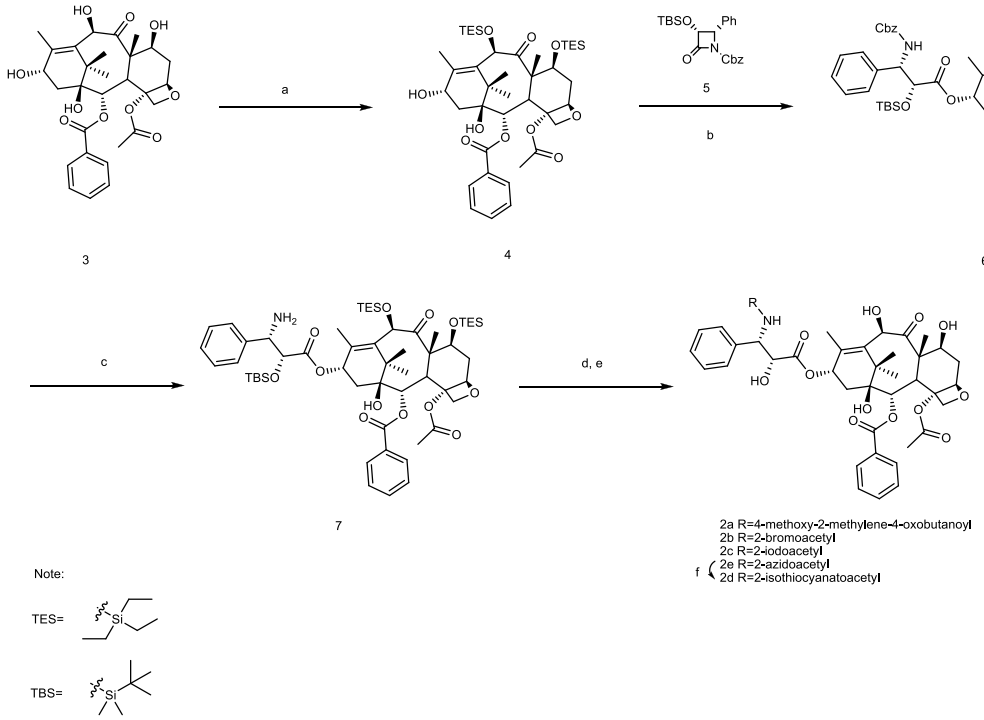

Scheme 1. Reagents and conditions: (a) TESCl, TEA, DMAP, LiBr, THF, r.t. to 70 °C, 84%; (b) LHMDS, THF, -45 °C, 79%; (c) 10% Pd/C, H_2, MeOH, 64%; (d) DCC, DMAP, acid, DCM, 0 °C to r.t.; (e) HF, Py, CH_3CN or 5% HCl/MeOH, 32% for **2a**, 40% for **2b**, 48% for **2c** and 83% for **2e** for two steps (d, e); (f) PPh_3, CS_2, THF, 83%.

Movie legends

Movie M1. Conformational transition from apo to baccatin III bound, unassembled tubulin state. Top view on β-tubulin (onto the "plus end" in the context of a microtubule).

Movie M2. Conformational transition from apo to baccatin III bound, unassembled tubulin state. Luminal view on β-tubulin (view from the lumen in the context of a microtubule).

Movie M3. Conformational transition from apo to **2a** bound, unassembled tubulin state. Top view on β-tubulin (onto the "plus end" in the context of a microtubule).

Movie M4. Conformational transition from apo to **2a** bound, unassembled tubulin state. Luminal view on β-tubulin (view from the lumen in the context of a microtubule).

Movie M5. MD movie of the apo tubulin dimer showing the occupancy of the taxane site by the βM loop. 1 μs simulation, 1 snapshot every 5 ns, βM loop in yellow.

Movie M6. Simulation of ligand exit and entry using targeted MD for baccatin III unbinding from and binding to αβ-tubulin.

Movie M7. Simulation of ligand exit and entry using targeted MD for paclitaxel unbinding from and binding to αβ-tubulin.

Supplemental Figures

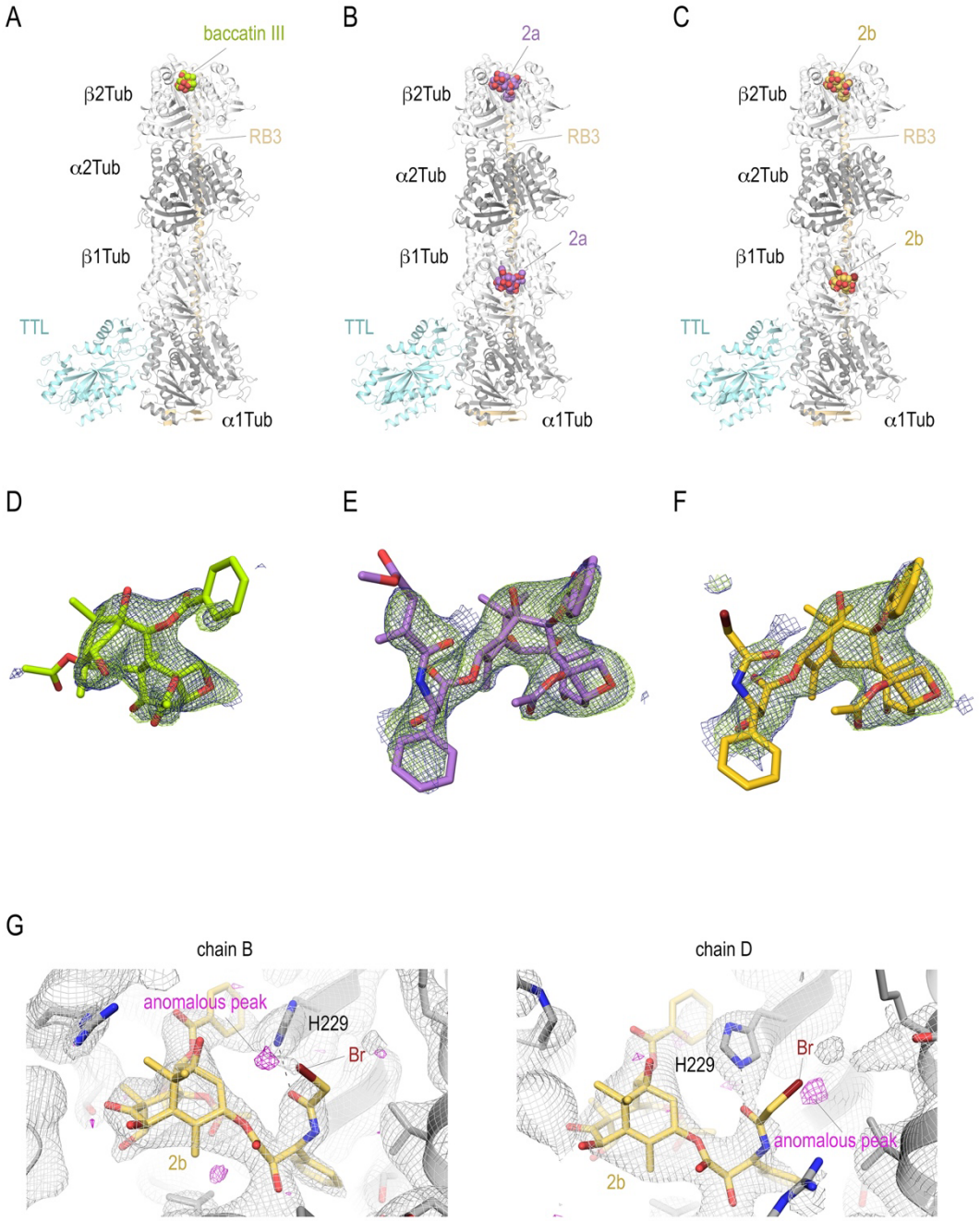

Figure S1. T_2R-TTL structures in complex with baccatin III, 2a, and 2b. Overall view of the T_2R-TTL-baccatin III **(A),** the T_2R-TTL-**2a** and **(B)**, and the T_2R-TTL-**2b** crystal structures. The α- and β-tubulin chains are colored in dark and light grey, respectively. The TTL chains (cyan) and the RB3 (yellow-orange) are shown in ribbon representation. The tubulin-bound ligands are displayed as spheres and are colored following the same color scheme as in the main figures. (**D-F**) Electron-density maps highlighting the bound baccatin III, **2a,** and **2b.** The SigmaA-weighted 2mFo - DFc (dark blue mesh) and mFo - DFc (light green mesh) omit maps are contoured at +1.0σ and +3.0σ, respectively. The map calculations excluded the atoms of the corresponding ligands. (**G**) Anomalous density peaks detected in both the binding sites in chains B and D of T_2R-TTL for the bromine moiety of compound **2b**.

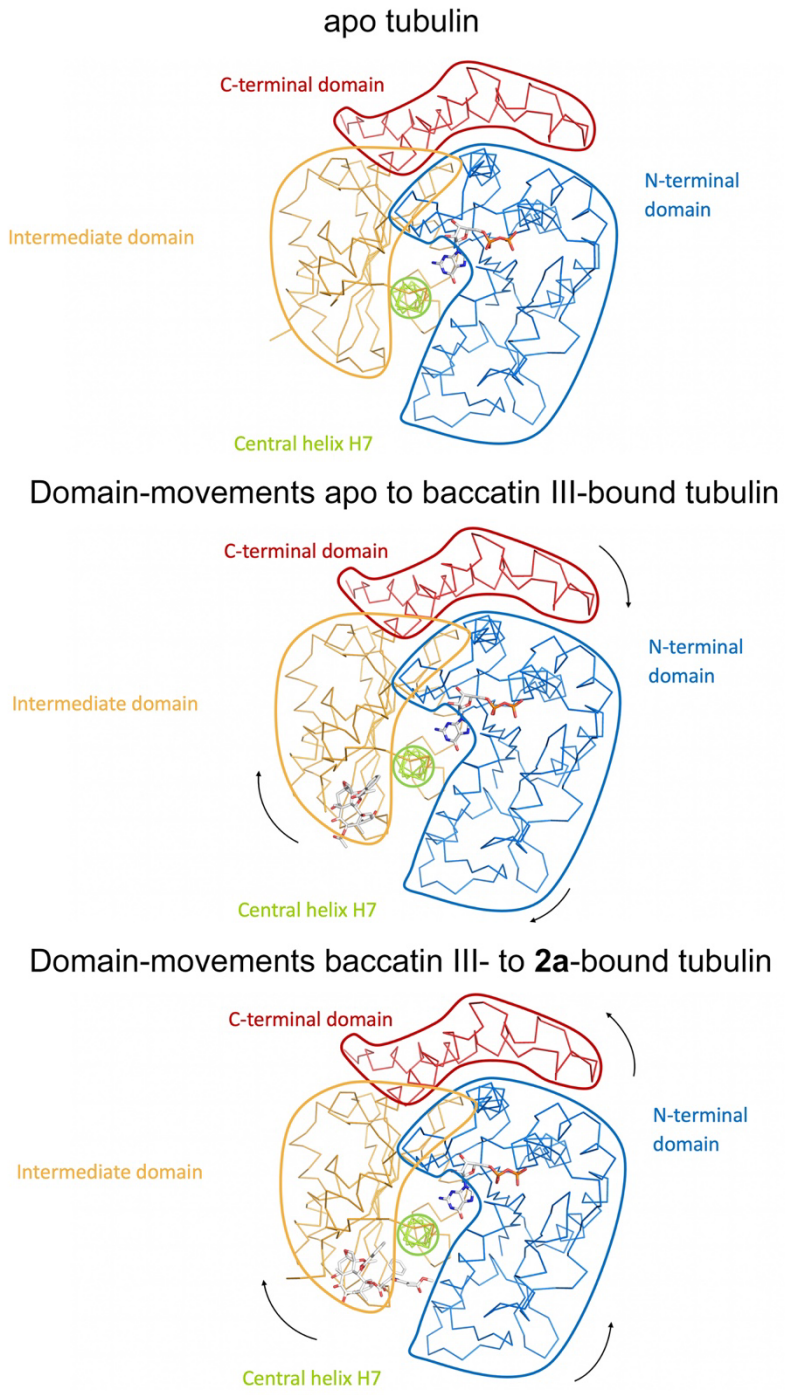

Figure S2. Schematic representation of subtle domain movements observed from apo to baccatin III- to 2a-bound curved tubulin. The three structures were superimposed onto their central helices βH7 to highlight better the subtle domain movements relative to each other. The individual domains are colored according to their domain assignment and their borders are contoured using the same color scheme: N-terminal domain (N-domain, marine blue), intermediate domain (I-domain, orange), central helix βH7 (lemon), C-terminal domain (C-domain, red). The directions of the individual movements are highlighted with black arrows.

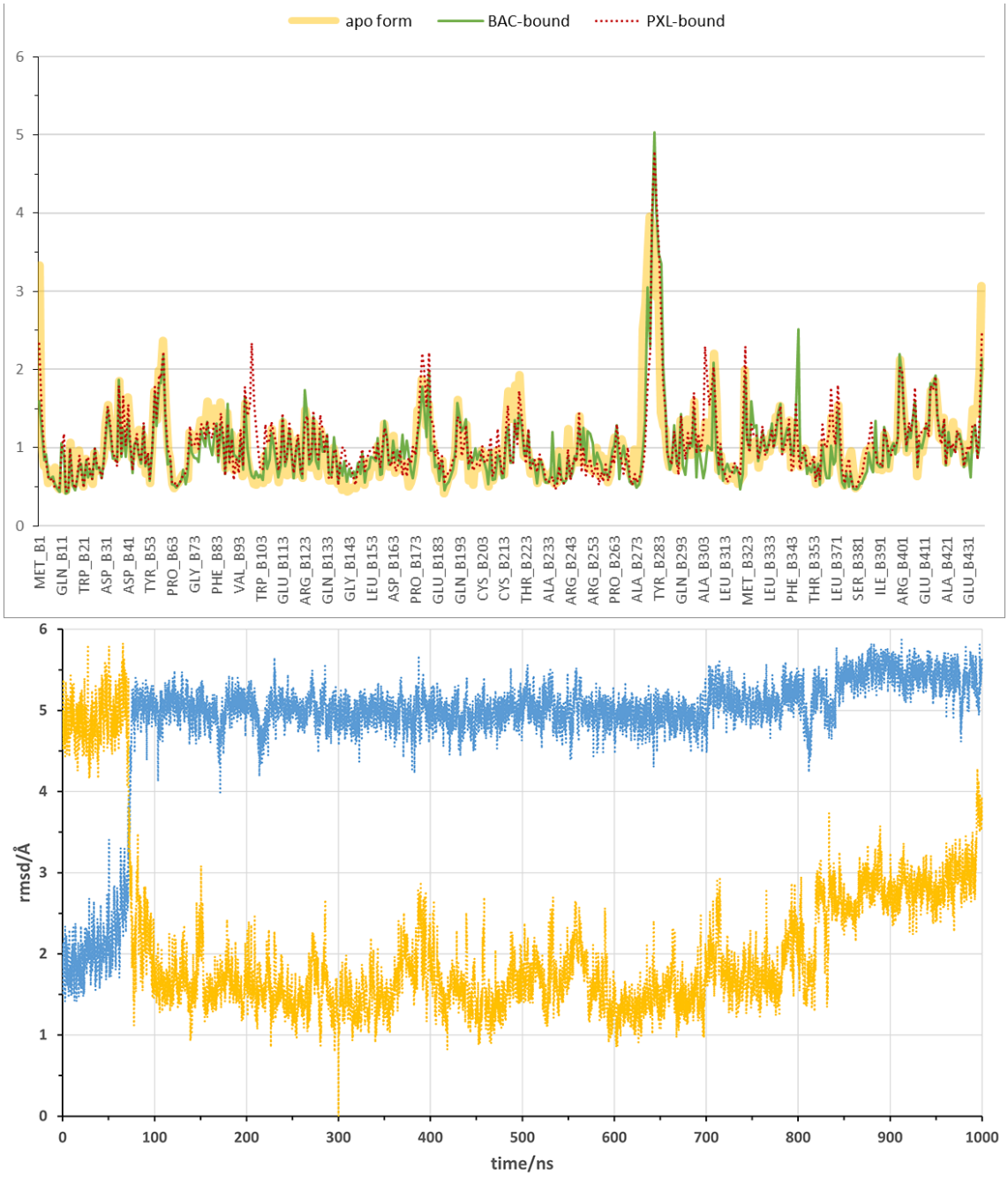

Figure S3. Flexibility of β subunit and βM loop during the αβ-tubulin dimer MD simulation. (Top) Mass-weighted positional fluctuations (or root-mean-square fluctuations, Å) by residue for atoms in the β subunit of the αβ-tubulin dimer over the course of 0.6 μs of MD simulation, in the apo form (yellow line) and in complex with baccatin III (green line) or paclitaxel (red dotted line). **(Bottom)** Evolution of the conformation of the βM loop in the 1.0 μs simulation of the αβ-tubulin dimer free in solution. The Cα root-mean-square deviation is measured with respect to either the initial α-helical structure (blue line) or the extended hairpin conformation that was stabilized at 300 ns (orange line).

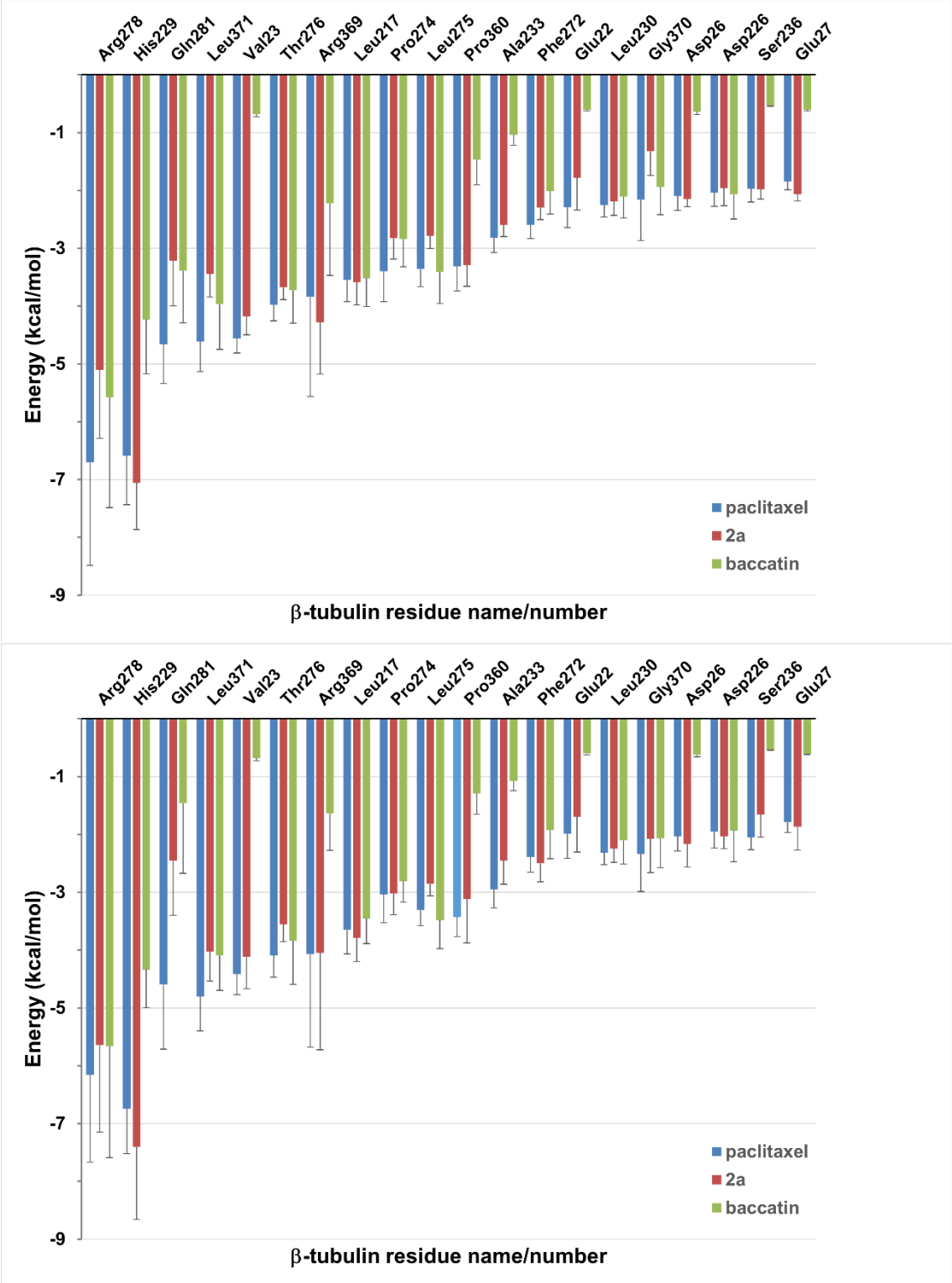

Figure S4.- Solvent-corrected interaction energies between individual β1-tubulin residues and ligands throughout the MD simulations of the minimalist representation of a microtubule. (**A**) The interfacial site 1 between neighboring protofilamentes. (**B**) The solvent-exposed site 2. These per-residue energies, which together represent a "binding fingerprint", were calculated by means of the program MM-ISMSA (*75*) using 120 complex structures from the MD simulations after equilibration (5-600 ns), cooling down to 273 K and energy minimization. A cut-off of 1.5 kcal mol^{-1} was used in the plot for enhanced clarity. Bars are standard errors.

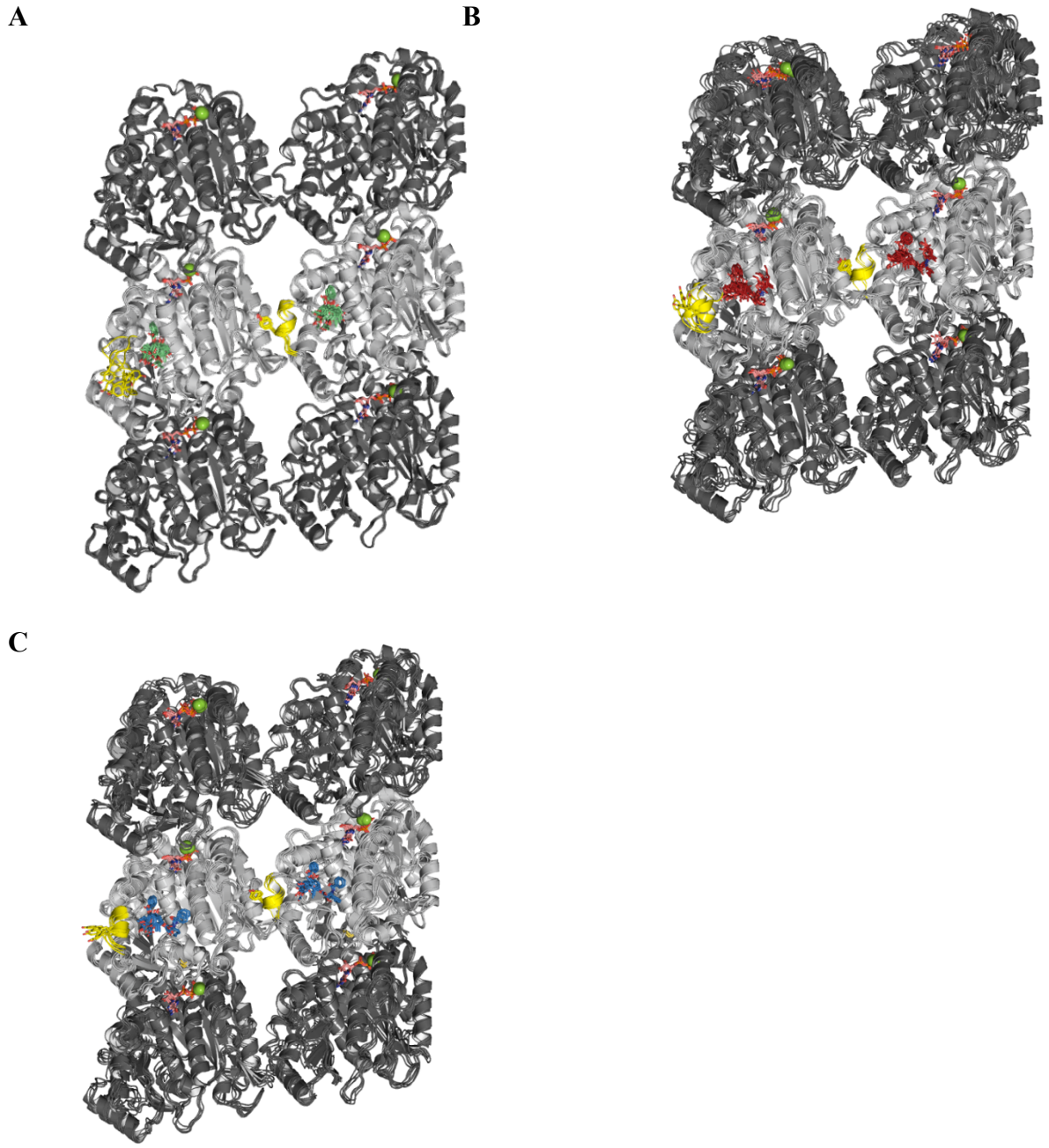

Figure S5.- MD simulations of minimalist representations of a microtubule ((α$_1$-β$_1$-α$_2$)/(α$_{1'}$-β$_{1'}$-α$_{2'}$)) in complex with baccatin III (green, A), 2a (red, B), or paclitaxel (blue, C). α- (dark grey) and β-tubulin (light grey) are displayed as ribbons, with the βM loop colored in yellow and the side chain of Tyr283 as sticks. GDP and GTP are shown as sticks, with C atoms colored in salmon. Mg^{2+} ions are displayed as green spheres. Each set of five overlaid structures represents a conformational ensemble made up of snapshots spaced by 5 ns taken from the equilibrated part of the trajectory and then cooled down to 273 K and energy minimized. Site 1 (at the top of each figure) is located at the interface between two neighboring protofilaments whereas site 2 (at the bottom of each figure) is devoid of any lateral contacts but exposed to the bulk solvent instead.